Are Further Cross Section Measurements Necessary for Space Radiation Protection or Ion Therapy Applications? Helium Projectiles

Citation for the original published paper (version of record):
Norbury, J., Battistoni, G., Besuglow, J. et al (2020). Are Further Cross Section Measurements Necessary for Space Radiation Protection or Ion Therapy Applications? Helium Projectiles. Frontiers in Physics, 8.
http://dx.doi.org/10.3389/fphy.2020.565954

frontiers
in Physics

REVIEW
published: 30 November 2020
doi: 10.3389/fphy.2020.565954

Are Further Cross Section Measurements Necessary for Space Radiation Protection or Ion Therapy Applications? Helium Projectiles

John W. Norbury[1]*, Giuseppe Battistoni[2], Judith Besuglow[3,4], Luca Bocchini[5], Daria Boscolo[6], Alexander Botvina[7], Martha Clowdsley[1], Wouter de Wet[8], Marco Durante[6,9], Martina Giraudo[5], Thomas Haberer[10], Lawrence Heilbronn[11], Felix Horst[6], Michael Krämer[6], Chiara La Tessa[12,13], Francesca Luoni[6,9], Andrea Mairani[10], Silvia Muraro[2], Ryan B. Norman[1], Vincenzo Patera[14], Giovanni Santin[15,16], Christoph Schuy[6], Lembit Sihver[17,18], Tony C. Slaba[1], Nikolai Sobolevsky[7], Albana Topi[6], Uli Weber[6], Charles M. Werneth[1] and Cary Zeitlin[19]

[1]NASA Langley Research Center, Hampton, VA, United States, [2]Istituto Nazionale di Fisica Nucleare (INFN), Sezione di Milano, Milan, Italy, [3]German Cancer Research Center (DKFZ), Heidelberg, Germany, [4]University of Heidelberg, Heidelberg, Germany, [5]Thales Alenia Space, Torino, Italy, [6]GSI Helmholtzzentrum für Schwerionenforschung, Darmstadt, Germany, [7]Institute for Nuclear Research of the Russian Academy of Sciences, Moscow, Russia, [8]University of New Hampshire, Durham, NH, United States, [9]Technische Universität Darmstadt, Darmstadt, Germany, [10]Heidelberg Ion Beam Therapy Center, Heidelberg, Germany, [11]University of Tennessee, Knoxville, TN, United States, [12]University of Trento, Trento, Italy, [13]Trento Institute for Fundamental Physics and Applications (INFN-TIFPA), Trento, Italy, [14]Universita' di Roma "Sapienza", Roma, Italy, [15]European Space Agency, Noordwijk, Netherlands, [16]RHEA System, Noordwijk, Netherlands, [17]Technische Universität Wien, Atominstitut, Vienna, Austria, [18]Chalmers University of Technology, Gothenburg, Sweden, [19]Leidos Innovations Corporation, Houston, TX, United States

The helium (^{4}He) component of the primary particles in the galactic cosmic ray spectrum makes significant contributions to the total astronaut radiation exposure. ^{4}He ions are also desirable for direct applications in ion therapy. They contribute smaller projectile fragmentation than carbon (^{12}C) ions and smaller lateral beam spreading than protons. Space radiation protection and ion therapy applications need reliable nuclear reaction models and transport codes for energetic particles in matter. Neutrons and light ions (^{1}H, ^{2}H, ^{3}H, ^{3}He, and ^{4}He) are the most important secondary particles produced in space radiation and ion therapy nuclear reactions; these particles penetrate deeply and make large contributions to dose equivalent. Since neutrons and light ions may scatter at large angles, double differential cross sections are required by transport codes that propagate radiation fields through radiation shielding and human tissue. This work will review the importance of ^{4}He projectiles to space radiation and ion therapy, and outline the present status of neutron and light ion production cross section measurements and modeling, with recommendations for future needs.

Keywords: helium projectile cross section measurements, space radiation cross sections, ion therapy cross sections, helium projectile ion therapy, helium projectile space radiation

OPEN ACCESS

Edited by:
Federico Giove,
Centro Fermi - Museo storico della fisica e Centro studi e ricerche Enrico Fermi, Italy

Reviewed by:
Loredana G. Marcu,
University of Oradea, Romania
Giacomo Cuttone,
Laboratori Nazionali del Sud (INFN), Italy

***Correspondence:**
John W. Norbury
john.w.norbury@nasa.gov

Specialty section:
This article was submitted to Medical Physics and Imaging, a section of the journal Frontiers in Physics

Received: *26 May 2020*
Accepted: *21 August 2020*
Published: *30 November 2020*

Citation:
Norbury JW, Battistoni G, Besuglow J, Bocchini L, Boscolo D, Botvina A, Clowdsley M, de Wet W, Durante M, Giraudo M, Haberer T, Heilbronn L, Horst F, Krämer M, La Tessa C, Luoni F, Mairani A, Muraro S, Norman RB, Patera V, Santin G, Schuy C, Sihver L, Slaba TC, Sobolevsky N, Topi A, Weber U, Werneth CM and Zeitlin C (2020) Are Further Cross Section Measurements Necessary for Space Radiation Protection or Ion Therapy Applications? Helium Projectiles. Front. Phys. 8:565954. doi: 10.3389/fphy.2020.565954

1 INTRODUCTION AND REVIEW

The International Biophysics Collaboration[1] (IBC) was recently formed at the GSI Helmholtzzentrum für Schwerionenforschung, with the aim of utilizing the future Facility for Antiproton and Ion Research (FAIR) and other accelerators for biophysics studies relevant to space radiation protection, ion therapy, and other biophysics applications. Within the IBC, a cross section working group has been formed to study what cross section measurements and modeling need to be performed to support the broad aims of the IBC. Membership of the cross section working group is open, and other colleagues are encouraged to participate: An important objective for the cross section working group is to have broad support within the international scientific community.

Previous analyses of experimental data [1–4] focused on measurement gaps for space radiation. The highest priority measurement recommendations were double differential cross sections for the following ion[2] reactions,

$$\mathrm{He, C, O, Si, Fe + H, C, O, Al, Fe} \rightarrow {}^{1,2,3}\mathrm{H}, {}^{3,4}\mathrm{He} + \mathrm{X}, \qquad (1)$$

where X is anything, thereby denoting an inclusive reaction, where a particular nuclide, say ^{2}H, is measured[3] along with anything (X) else. The projectiles He, C, O, Si, and Fe were chosen[4] because of their prominence in the free space galactic cosmic ray (GCR) spectrum. The targets H, C, O, Al, and Fe were chosen as being representative elements in the human body and spacecraft. For applications in ion therapy, projectiles ranging from H to O interacting with targets composed of H, C, and O as main constituents of the human body are typically considered crucial. Therapy facilities employing H and ^{12}C in the energy range of a few hundred MeV/n have been in use for many years around the world, whereas ions such as ^{4}He and ^{16}O are considered important extensions of the currently offered treatments [6]. Consequently, the needs of space radiation protection can be seen as a superset encompassing the needs of therapy applications in most cases, due to the significantly larger range of projectile, energy, and target combinations of interest for the space radiation community [7].

The aim of the present study was therefore to consider whether further cross section measurements are necessary for space radiation protection or ion therapy applications, define overlaps in interest for both disciplines, and prioritize needed experiments and measurement quantities.

1.1 Importance of Light Ion Fragments

In the context of space radiation protection, light ion fragments ^{1,2,3}H and ^{3,4}He were emphasized [1–4] for future double differential cross section measurement recommendations in **Eq. 1** for the following reasons:

1. Neutrons and light ion fragments dominate dose equivalent [8–10] for realistic spacecraft shield thicknesses ($\geq$ 20 g/cm^2). This can be seen in **Figure 1**, which shows the contribution to blood-forming organ dose equivalent for free space, simple geometries, and various spacecraft locations.
2. Because they have small charge and mass, neutrons and light ion fragments are scattered at large angles, and therefore require full 3-dimensional transport [11] methods (as opposed to 1-dimensional straight-ahead scattering approximations). Full 3-dimensional transport methods, in turn, require nuclear physics double differential cross sections [12, 13] as input.
3. Transport code (GEANT, FLUKA, MCNP, PHITS, HZETRN, and SHIELD) comparisons [14] show the largest differences for light ion fragment production. The disagreements are mainly due to inaccurate light ion nuclear physics models and lack of experimental data to be used to improve these models. As an illustration of this, **Figure 2** shows large disagreements for numerous transport code comparisons for the production of ^{3}H and ^{3}He.
4. An experimental double differential cross section measurement program was recently completed at the NASA Space Radiation Laboratory (NSRL), located at Brookhaven National Laboratory (BNL), using oxygen and iron beams on several targets, with the production of light ion fragments [16]. Large differences were seen between measurements and the light ion cross-section models used in the PHITS [17] transport code.
5. An experimental thick target program was also recently completed at the NSRL, using unique combinations of double thick targets where incident beam particles scattered from the first target and secondary fragments subsequently scattered from a back target. This simulated the scattering geometry in a spacecraft, where fragments are produced when GCRs interact with a spacecraft wall and more scattered products are produced from the far, back, and surrounding walls. These measurements show significant discrepancies [18] compared to transport codes (MCNP and PHITS) for light ions. Further cross section measurements of light ion fragments have been recommended to resolve these discrepancies.
6. Mars Science Laboratory Radiation Assessment Detector (MSL-RAD) light ion flux measurements highlight the

---

[1] Spokesperson: Vincenzo Patera (Universita' di Roma "Sapienza", Roma, Italy).

[2] The very first ion collision experiments [5] were carried out more than 100 years ago by Ernest Rutherford, who scattered helium (He) projectiles (alpha particles) from gold (Au) targets. Of course, no accelerators were available, and the helium projectiles were produced from the radioactive decay of radium. The helium projectile kinetic energy was only 5 MeV (about 1 MeV/n) and the scattering was elastic (no fragments could be produced), but some of the helium projectiles suffered large deflections from the incident direction, which indicated scattering from a tiny atomic core. This was the discovery of the atomic nucleus, with a size of order 10 m. Helium projectiles are also the subject of the present work.

[3] An exclusive measurement would mean that ^{2}H is measured as well as all other possible reaction products. Note that an inclusive measurement is the sum of all exclusive measurements.

[4] He($Z = 2$), C($Z = 6$), O($Z = 8$), Si($Z = 14$), Fe($Z = 26$).

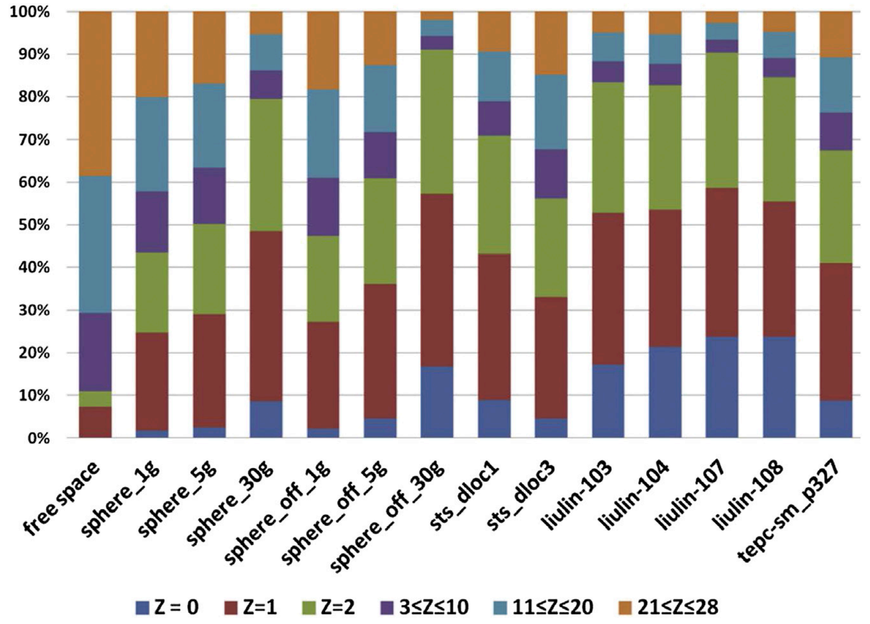

FIGURE 1 | Calculated percent contribution to blood-forming organ (BFO) dose equivalent for free space (far left), simple spherical geometries in free space, and detector locations inside the space shuttle (STS) and the International Space Station (ISS) in free space. The vehicles included three aluminum spheres with areal densities 1, 5, and 30 g/cm^2 where the body was placed at the center of the sphere (sphere_1g, sphere_5g, and sphere_30g) and three spheres of the same areal densities where the body was placed against the wall of the sphere (sphere_ off_1g, sphere_off_5g, and sphere_off_30g). For the latter cases, the spheres were constructed so that they would each have the same habitable volume as the Multi-Purpose Crew Vehicle (MPCV), 316 cubic feet (8.95 m^3). Thus, each sphere had an inner radius of 1.288 m. Also, six locations were studied in the STS (shuttle) where detectors have historically been placed (sts_dloc1-6). Five locations in the ISS 6A configuration were also used: two points in the Destiny (Lab) module laboratory area (Liulin_103, Liulin_107); two points in the Unity (Node1) module (Liulin_104, Liulin_108); and one point in the Zvezda (SM; service module) module on panel number 327 (TEPC-sm_p327). Reprinted from Walker et al. [8].

need for improved nuclear interaction models. Light ion model results show moderate to large discrepancies [19–21] over the MSL-RAD energy range,[5] with model errors mainly attributed to inaccurate light ion nuclear physics models.

(7) Calculations with the HZETRN transport code underpredict dose measurements from the International Space Station [22, 23], at high latitudes where GCRs contribute most. The cause of the discrepancy has yet to be fully clarified, but improvements to the underlying cross section models will help remove some measure of uncertainty.
(8) Light ion cross sections represent the largest physics uncertainty in space radiation.
(9) Light ion cross section measurements [1] are needed to improve inaccurate light ion nuclear physics models.
(10) Light ion cross section measurements represent the largest gap in the cross section database [1].

The importance of light fragments, and nuclear fragmentation in general, follows a similar rationale in ion therapy as for space radiation and was already discussed previously [24–26].

(1) Base data used for treatment planning are typically generated using either Monte Carlo [27, 28] or dedicated deterministic [29, 30] transport codes. Therefore, the physical models used in each transport code directly translate to the quality of a treatment, especially for “novel” ions [31–33].
(2) Inter-code comparisons of Monte Carlo transport codes show important differences for the spatial distributions of prompt gamma rays, light charged fragments, and neutrons [34].
(3) Heavier projectiles, like ^{12}C, undergo significant amounts of nuclear fragmentation along their beam path, and the lighter fragments produced deposit a significant dose behind the Bragg peak (fragment tail) [35].
(4) Light fragments are of special interest for online monitoring purposes in ion beam therapy [36].
(5) If the projectile fragmentation cross sections are not precisely modeled, then dose calculation algorithms become inaccurate, which can lead to inhomogeneous dose distributions and underdosage or overdosage of tumor sites [37].

---

[5] In this particular case, the observed discrepancies did not contribute significantly to dose-equivalent, but improvements would yield better agreement with MSL-RAD.

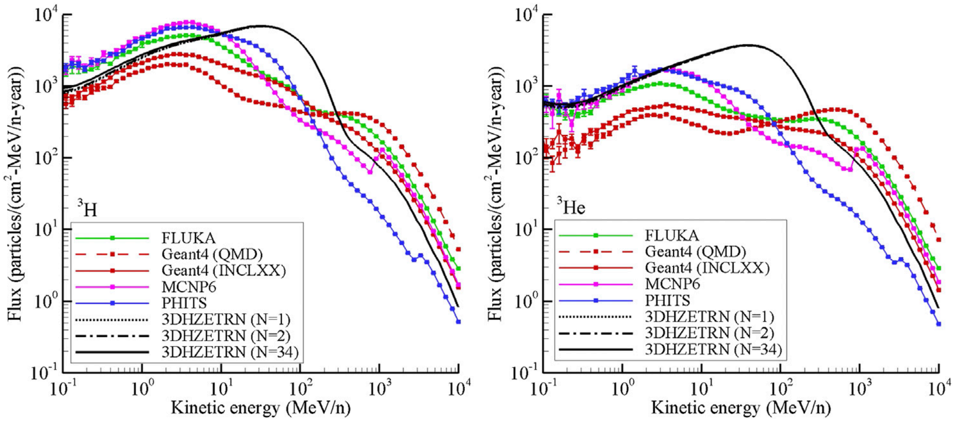

FIGURE 2 | ^{3}H and ^{3}He flux behind 60 g/cm^2 Al shield for GCR minimum spectrum. Reprinted from Slaba et al. [15].

(6) In addition to projectile fragmentation, fragmentation of the target is also highly relevant for precise dose calculations in ion therapy [38].

As emphasized above, light ions make large contributions to dose equivalent and are essential for treatment planning, but the physics of their production remains poorly understood. One would hope to compare theoretical nuclear physics models to cross section measurements to resolve these issues, but the largest gap in the cross section database occurs for light ions. This is why a further cross section measurement program is recommended for space radiation and ion therapy applications.

1.2 Importance of Double Differential Cross Sections

Neutrons and light ion fragments are scattered at large angles because they have small charge and mass. They therefore require full 3-dimensional transport methods, which need double differential cross sections [12, 13] as input. This is why double differential[6] cross sections are highlighted in the present work, with emphasis on isotopic production cross sections, $d^2\sigma/dEd\Omega$, where E is the total energy of a fragment given[7] by $E \equiv T + m$, where T is the kinetic energy and m is the rest mass.[8] The fragment solid angle is Ω.

Other reasons for emphasizing double differential isotopic cross sections are as follows. Single differential spectral, $d\sigma/dE$, and angular, $d\sigma/d\Omega$, cross sections can be obtained from $d^2\sigma/dEd\Omega$ by integrating over angle or energy as in $d\sigma/dE = \int d\Omega(d^2\sigma/dEd\Omega)$ and $d\sigma/d\Omega = \int dE(d^2\sigma/dEd\Omega)$. Total cross sections are obtained *via* $\sigma = \int dEd\Omega(d^2\sigma/dEd\Omega)$. Therefore, from a theoretical point of view, if one would measure a complete set of double differential cross sections, then one could generate all necessary single differential and total cross sections. In practice, this is typically not feasible. However, there are examples of systematic measurements of double differential fragmentation cross sections of light projectiles on different thin targets, for example, with 50 MeV/n (3°–39°) and 95 MeV/n (4°–39°) ^{12}C beams [39–41] performed at GANIL. As usual, this experimental setup does not cover the entire spectrum of fragment information (mass, charge, energy, and angle). Especially for heavier projectile, there are large gaps in the published data. Therefore, future experimental programs should focus on measuring double differential cross-section data sets as completely as possible (covering all angles, energies, and fragments including neutrons) to be able to cross-check them against measured total and single differential cross sections. The single differential data could be efficiently measured by accompanying experiments.

Similar reasoning applies to isotopic fragment cross sections vs. elemental or charge changing cross sections. Consider light ions: An isotopic measurement would provide double differential production cross sections for each ^{1}H, ^{2}H, ^{3}H, ^{3}He, and ^{4}He, whereas elemental measurements only provide cross sections for H and He. Yet, the elemental cross sections can all be obtained from the isotopic cross sections by adding the individual isotopic contributions. Isotopic cross sections cannot be obtained from elemental measurements. Again, some applications require only elemental or charge changing cross sections, and some require isotopic cross sections. It therefore makes sense to focus future measurements on attaining isotopic resolution so that the cross sections are useful for all possible future applications. Of course, isotopic double differential cross sections are more difficult to measure than, for example, charge changing total cross sections. However, given the very broad range of future applications of cross section measurements covering both space radiation and ion therapy, it is deemed worthwhile to focus future measurements on isotopic double differential cross sections.

---

[6] Other double differential cross sections, such as Lorentz-invariant double differential cross sections or double differential cross sections written in terms of momentum, transverse momentum, etc., are equivalent to $d^2\sigma/dEd\Omega$.

[7] Unless specified otherwise, standard particle physics units are used in the text, with the speed of light defined as unity, $c \equiv 1$. This is why the total energy is written as $E \equiv T + m$ and not $E \equiv T + mc^2$.

[8] Note that $dE = dT$. Most experiments measure differential cross sections as a function of T.

All of the above discussion in this subsection has centered on measurement issues, but the same is true for theoretical modeling. At the most fundamental level, a particle physics Feynman diagram gives the quantum mechanical amplitude for a given process which is inserted directly into a formula for the double differential cross section. Spectral, angular and total cross sections are obtained by integrating as described above. Even if one is not using Feynman diagrams directly, the quantum mechanical amplitude, obtained by some theoretical model, is the most fundamental quantity. In other words, double differential cross sections are most fundamental. Another matter concerns comparing theoretical model results to experimental measurements. Comparisons of double differential cross section models with double differential cross section measurements is the most precise sort of validation test of a theoretical model. Comparing theoretical models for single differential spectral or angular cross section measurements is less precise: The models might get these correct, even though the underlying double differential cross sections might be incorrect. Comparing total cross section models with experiment is the least precise. In summary, the most precise test of a theoretical model is comparison of double differential cross sections with experiment. If these are correct, then single differential spectral and angular cross sections, as well as total cross sections, will automatically be correct. The reverse situation does not hold; for example, comparing total theoretical model cross sections with experiment will not guarantee that the double differential cross sections are correct. The considerations are the same for isotopic vs. elemental cross sections. If all the theoretical model isotopic cross sections agree with experiment, then the elemental and charge changing cross sections will automatically be correct as well. The reverse situation does not hold.

However, it is important to note that in many modern Monte Carlo transport codes, the removal of primary ions and the fragment production are treated separately. The interaction probability is typically sampled according to parameterized total reaction cross sections for which semi-empirical models fine-tuned to experimental data are used, while the fragment production and their double differential distribution is obtained from nuclear event generators and coalescence/evaporation models. Therefore, to optimize such transport codes, experimental data on both the total reaction cross section and the double differential fragment distributions are required.

The conclusion of this subsection is that the most useful and precise types of cross sections are isotopic double differential cross sections. This is true for both experimental measurements and theoretical models. If these types of cross sections give good comparisons between models and experiment, then all other types of cross sections will automatically also give good comparisons. Also, all other types of cross sections (both theoretical and experimental) can be obtained from isotopic double differential cross sections. This behavior should be exploited to cross-check total and single differential datasets.

1.3 Measurements

Previous measurement studies [1–4] will now be summarized, for all types of projectiles, emphasizing double differential cross sections for light ion fragment production. **Figures 3–7** show where isotopic double differential cross section data have been measured for light ion production. The following conclusions can be stated:

- In the low energy region below the pion threshold (< 280 MeV/n), double differential cross sections for light ion production mainly exist for H, He, C, O, Ne, and Ar[9] projectiles.
- In the medium energy (280–3,000 MeV/n) region, double differential cross sections for light ion production mainly exist for H, He, C, Ne, and Ar projectiles.
- In the high energy (3–15 GeV/n) and very high energy ($>$ 15 GeV/n) regions, there are no double differential cross-section data[10] for light ion production.
- Even though there are a moderate number of experimental measurement articles dealing with helium projectiles, further detailed analysis of He data below 3 GeV/n reveals significant problems and flaws with the data, leading to the conclusion that there is almost no high-quality double differential data for helium projectiles over the entire energy region.[11] This is discussed in more detail later in this article.
- No double differential cross section data exist for light ion fragment production from helium projectiles above 3 GeV/n.
- No double differential cross section data exist for light ion fragment production from oxygen projectiles[12] above the pion threshold (> 280 MeV/n).
- No double differential cross section data exist for light ion fragment production from silicon (Si) projectiles in any energy region.
- No double differential cross section data exist for light ion fragment production from iron (Fe) projectiles[13] in any energy region. This is particularly surprising, given the prominent role of Fe projectiles in space radiation biophysical studies [44].

1.3.1 Measurement Strategies and Experimental Setup

When planning and setting up measurements of double differential cross sections, there are a number of factors to be considered, ranging from detector system, detection efficiency,

---

[9] Ne($Z = 10$), Ar($Z = 18$).

[10] Except for proton + target $\rightarrow$ proton + X.

[11] A set of total cross sections for helium ions in the therapeutic energy range was recently measured within the scope of their application in ion therapy [42, 43].

[12] This situation is currently being partially addressed. An article describing a new set of measurements for O projectiles at 300 MeV/n is currently in preparation [16].

[13] This situation is currently being partially addressed. An article describing a new set of measurements for Fe projectiles at 600 MeV/n is currently in preparation [16].

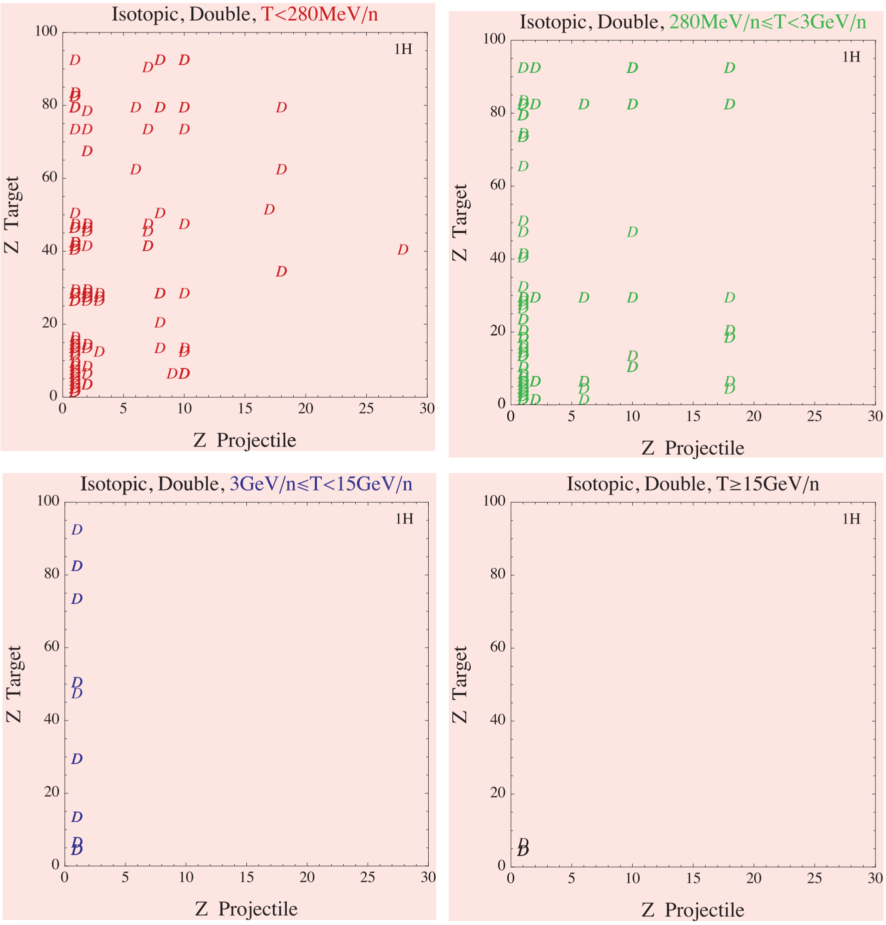

FIGURE 3 | Available isotopic double differential cross section measurements for ^{1}H fragment production. The symbol D represents where a measurement has occurred. Projectile kinetic energies, T, are listed at the top of each panel. Reprinted from Norbury et al. [1].

statistics, beam monitor, acceptance angles, data acquisition system, target thickness, and time resolution for TOF (time of flight) techniques.

In order to measure the angular distributions, several different configurations are possible. One standard option is a TOF setup with a fast counting detector (e.g., plastic scintillator, silicon detector, and diamond detector) that provides trigger information, that is, the start signal, before the target, and a plastic scintillator, for example, some distance downstream from the target, providing the stop of the TOF, and measurements of the energy loss. After this, a thick dense crystal calorimeter (e.g., BGO and NaI) can be located to provide the projectile fragment residual energies. Additional detector systems can be added to this general setup to improve its capabilities. Tracking detectors in front and after the target allow vertexing and different magnet configurations, and large-area drift chambers behind the target can be employed to increase particle identification performance. Silicon detectors in different configurations, for example, silicon micro-strips or silicon pixel detectors, or emulsion chambers, can also be used. Time resolution between the start detector and the stop detector and the angular acceptances are important. To obtain the double differential cross sections, in addition to the angular distributions, the energy distributions also need to be determined at each point of the angular distributions.

In principle, all cross sections should be measured in targets with infinitesimal thickness, which are, however, not optimal from the experimental point of view since targets which are too thin increase the beam time requirements and increase susceptibility to systematic errors. The target thicknesses are therefore a trade-off between thick enough to give acceptable statistics when exposed during a reasonable time, but not so thick to give rise to substantial corrections for secondary and higher-order interactions in the targets. Targets should also not be thick enough to cause a significant decrease of the projectile energies in the target, since the cross sections are energy dependent. Measured fragment yields need to be converted to cross sections and require correction for the finite depth target which is applied to the cross section values of each fragment. The corrections are typically of the order of half the fraction of an interaction length presented by the target to the primary. For example, for a target depth of 20% of an interaction length, about 20% of the incident primary particles undergo a charge-changing

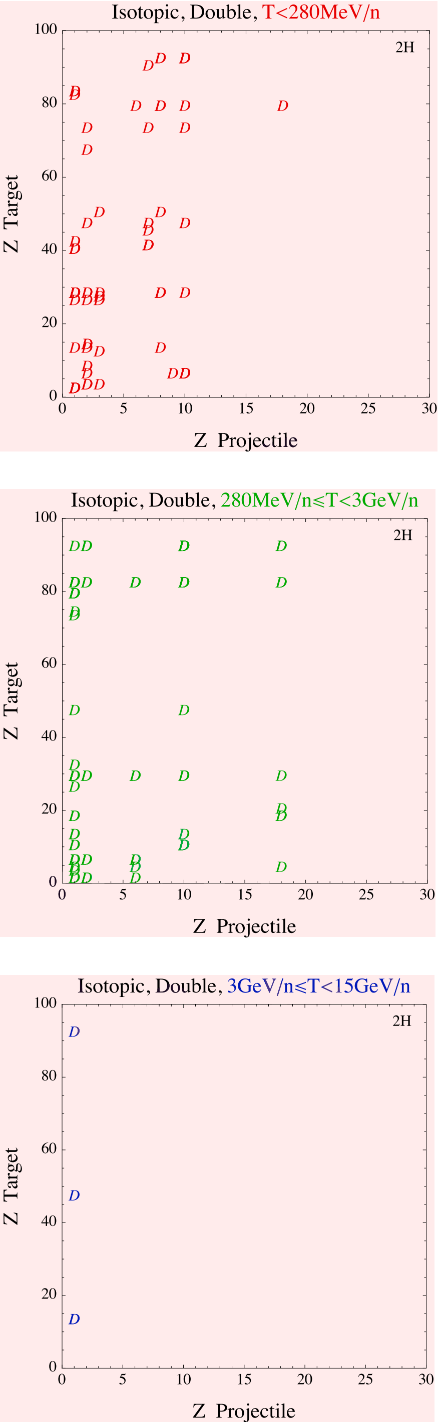
Isotopic, Double, T<280MeV/n

Isotopic, Double, 280MeV/n≤T<3GeV/n

Isotopic, Double, 3GeV/n≤T<15GeV/n

FIGURE 4 | Available isotopic double differential cross section measurements for ^{2}H fragment production. The symbol D represents where a measurement has occurred. Projectile kinetic energies, T, are listed at the top of each panel. No measurements are available above 15 GeV/n, which is why the bottom right panel is blank. Reprinted from Norbury et al. [1].

interaction in the target, and therefore about 10% of the fragments within a few charge units of the primary will undergo secondary charge-changing interactions. For experiments with a heavy projectile, the corrections for lighter fragments are more complicated, because they are both depleted by interactions in the target and are also produced as third- and higher-generation fragments by interactions of heavier fragments as they traverse the target.

It is always important to certify that particles created in other materials in the beam line are not measured. It is therefore essential that the beam never hits anything other than the target. When measuring neutron energy distributions, this is especially important since the neutron detectors are also picking up neutrons that scatter around the room before striking the detectors. Because their flight paths are unknown, those neutrons must be subtracted from the data. Measurements of the room-scattered neutrons should therefore be performed and subtracted from the total detected neutrons. Depending on the setup, this can be done by placing a shadow bar (a long, solid piece of iron, or other material, thick enough to stop the neutrons that enter it) directly between the target and the neutron detector, so that all neutrons originating from the target are blocked, and only room-scattered neutrons are detected. By subtracting the neutrons measured during the shadow bar run from the non-shadow bar run, the neutrons originating from the target can be determined. It is important to note that all of the previously mentioned experimental techniques do not scale well with increasing primary particle energy due to, for example, the inability to stop the light fragments in a crystal calorimeter or the increasing demands on TOF resolution and distance.

2 IMPORTANCE OF HELIUM PROJECTILES

2.1 Space Radiation

A discussion of the importance of helium projectiles in the galactic cosmic ray environment now follows.[14] Subsequent to the analyses of measurement gaps [1–4] discussed in **Section 1.3**, an important work was published by Slaba and Blattnig [46], which analyzed the contributions of each external boundary condition GCR ion to effective dose. Not only was the charge number (Z) contribution specified but also the energy range contributing to effective dose. Previous studies [1–4] emphasized measurement gaps, but the study of Slaba and Blattnig [46] enabled one to prioritize which measurement gaps were the most important ones to close for space radiation. **Figure 8** shows how helium projectiles dominate the effective dose contribution compared to heavier projectiles over the GCR energy region. For Al shield thickness of 20 g/cm^2, the study of Slaba and Blattnig [46] showed the following results at solar minimum:

- 86% of effective dose is contributed from GCR ions with kinetic energy $>$ 500 MeV/n.
- 50% of effective dose is contributed from GCR ions with kinetic energy $>$ 1.5 GeV/n.

---

[14] Helium projectiles are absent from the geomagnetically trapped radiation environment. They are present in solar particle events [45], but are of insufficient flux to make any significant contribution to the space radiation field.

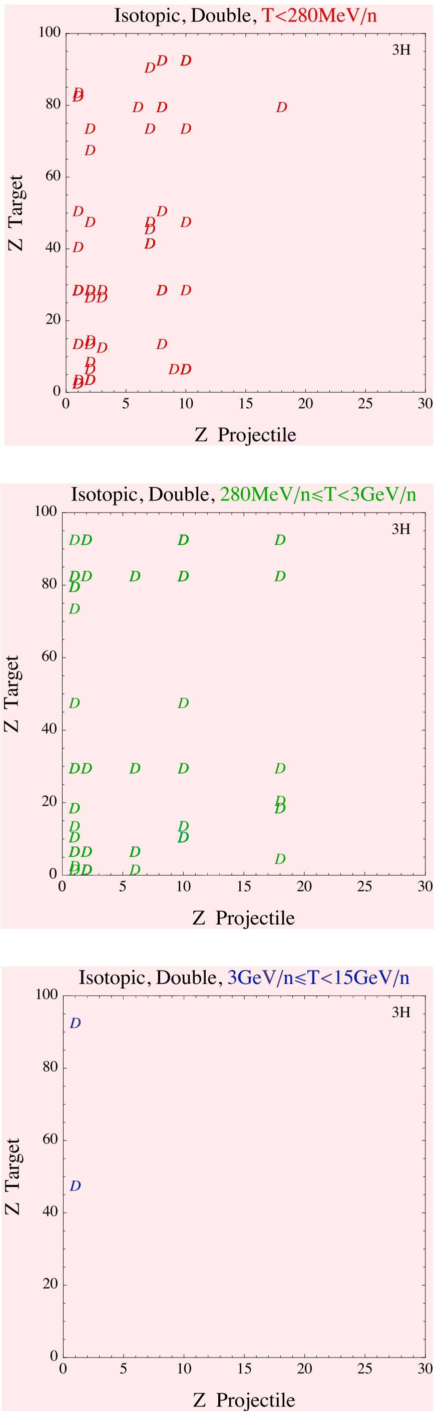

FIGURE 5 | Available isotopic double differential cross section measurements for ^{3}H fragment production. The symbol D represents where a measurement has occurred. Projectile kinetic energies, T, are listed at the top of each panel. No measurements are available above 15 GeV/n, which is why the bottom right panel is blank. Reprinted from Norbury et al. [1].

- 32% of effective dose is contributed from ions with $Z > 1$.
- He contribution to effective dose is 30% of the total ion ($Z > 1$) effective dose.

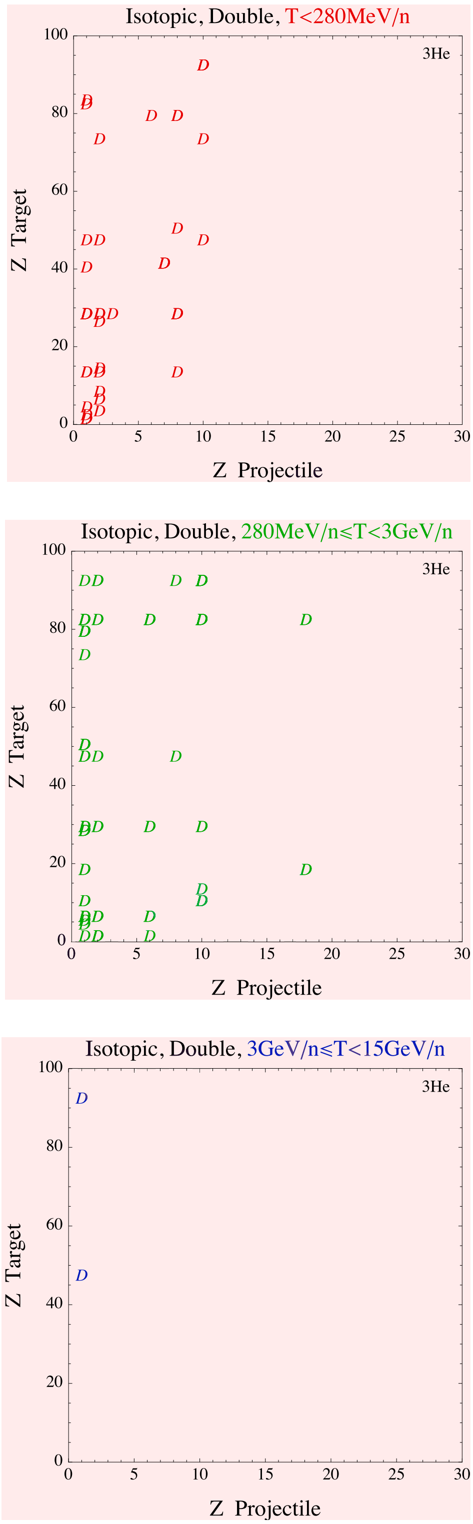

FIGURE 6 | Available isotopic double differential cross section measurements for ^{3}He fragment production. The symbol D represents where a measurement has occurred. Projectile kinetic energies, T, are listed at the top of each panel. No measurements are available above 15 GeV/n, which is why the bottom right panel is blank. Reprinted from Norbury et al. [1].

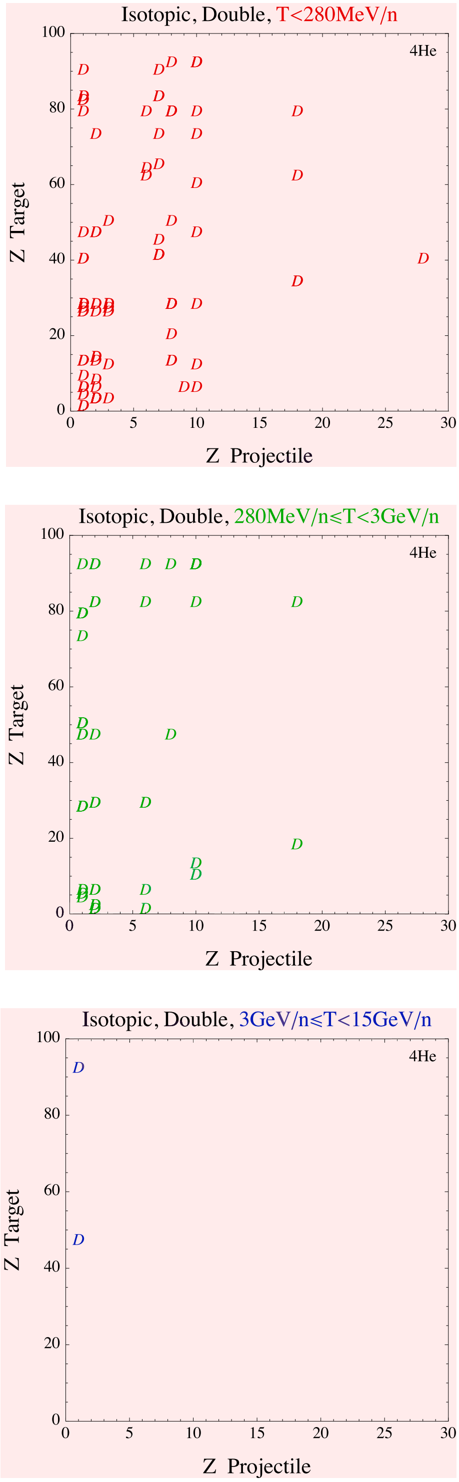

FIGURE 7 | Available isotopic double differential cross section measurements for ^{4}He fragment production. The symbol D represents where a measurement has occurred. Projectile kinetic energies, T, are listed at the top of each panel. No measurements are available above 15 GeV/n, which is why the bottom right panel is blank. Reprinted from Norbury et al. [1].

- He contribution to effective dose is 12% of the total effective dose (from all Z).

For Al shield thickness of 40 g/cm^2,

- 90% of effective dose is contributed from GCR ions with kinetic energy $>$ 500 MeV/n.
- 60% of effective dose is contributed from GCR ions with kinetic energy $>$ 1.5 GeV/n.
- He contribution to effective dose is 46% of the total ion ($Z > 1$) effective dose.
- He contribution to effective dose is 14% of the total effective dose (from all Z).

Using the calculations of reference [46], **Table 1** shows the percent contribution of each energy range to total He effective dose from the external GCR spectrum. For a shield thickness of 20 g/cm^2, all energy regions need to be covered, whereas for thicker 40 g/cm^2 shielding, only energies above 250 MeV/n are important. The following important conclusions can now be stated.

- More than half of the effective dose delivered by all GCR ions (including protons, i.e., $Z \geq 1$) is in the high energy region $>$ 1.5 GeV/n. Yet, this is the energy region with the largest measurement gaps.
- Of all external GCR ions heavier than protons ($Z \geq 2$), helium contributes more than any other individual ion to effective dose, with almost half of the contribution in the high energy region $>$ 1.5 GeV/n.

Also, similar results have been obtained by Bocchini et al. [47] obtained using Geant4. In particular, for Al thickness of 20 g/cm^2:

- 57% of male effective dose is contributed from GCR ions with kinetic energy higher than 1 GeV/n and about 24% of the dose is delivered by ions with $E > 3$ GeV/n.
- About 55% of the male effective dose due to GCR He particles is delivered by particle with energies greater than 1 GeV/n.
- GCR proton contribution to the male effective dose is about 57%, while the He contribution is about 19%, and all other ions (up to ^{56}Fe) contribute 24% of the total dose.
- He contribution to the male effective dose is 43% of the total ion $Z > 1$ effective dose.

However, at 40 g/cm^2 shielding thickness, the He particle with energies greater than 1 GeV/n represents 67% of the total male effective dose deposition due to GCR He particles, and most of the dose is deposited by particles in the energy range 1.5 GeV/n to 3 GeV/n. For thickness greater than 40 g/cm^2, the contribution of He particles with energies above 3 GeV/n also becomes significant. Differences in results can be due to the different simulations methods between the two works: HZTREN for [15, 23] and GRAS [48] in the latter case.

Extensive simulations have been performed by Bocchini et al. [47] to iteratively characterize the GCR contribution to the effective dose with Geant4, and here, results for He are reported. An aluminum spherical shell was modeled in GRAS [48], with varying thickness (i.e., from 10 up to 100 g/cm^2), and interplanetary GCR particles were isotropically generated, using the Badhwar-O'Neill 2010 model in 1977 solar minimum condition, with energies up to 100 GeV/n. Geant4 QGSP_BIC physics list was used, and a sensitivity study varying the physics list has been conducted. Effective dose has been calculated on a virtual scoring volume placed in the middle of the spherical shell, ICRP Publication 123 fluence to dose conversion factors [49] have been used, with NASA quality factors.

Figure 9 shows the male effective dose deposited by primary GCR He (including its secondary particles), while the percentage contribution of the different particle species to the dose is shown in **Figure 10**. The increase in the dose with thickness is in line with results reported in 50 for dose reduction of 1 GeV/n He particles against different spacecraft materials. At 30 g/cm^2, about 60% of the male effective dose is provided by secondary particles, mostly neutrons and protons, as shown in **Figure 10**. While in a low shielded scenario, representative for the first manned mission in the Lunar gateway, most of the He contribution to the dose is delivered by primary alpha particles, characterized by higher RBE values.

Geant4 simulations were also carried out to calculate the GCR He contribution to the dose in terms of energy range of the primary particle responsible for the dose deposition, to better prioritize testing activities. **Figure 11** shows the dose delivered by GCR helium particles in Sv/y per different thicknesses, considering both primary He and its generated secondary particles. For all thicknesses, the majority of the dose delivered by He is in the following energy ranges: 200–500 MeV (20–28% of total He dose) and 1.5–3 GeV/n (17–25% of total He dose), contributing overall to about 50% of the dose. Based on these results, availability of nuclear interaction cross section data for He in the 500 MeV/n–3 GeV/n energy range interacting with spacecraft materials should be a priority for space research, allowing transport code optimization.

2.2 Heavy Ion Therapy

After the treatment of more than 2000 patients with ^{4}He at the 184 inch synchrocyclotron and at the Bevalac in Berkeley [51], the interest of the therapy community shifted to the technically less demanding protons [52] and to the higher biological effectiveness offered by carbon ions [53, 54] instead. However, ^{4}He has physical and biological properties in between the protons and carbon ions currently in use. It is being considered as a clinical beam at the Heidelberg Ion Beam Therapy Center (HIT). Preclinical evaluation studies showed promising indications in the application of helium beam therapy, especially in pediatric patients [55] and tumors growing in close proximity to multiple organs at risk (OARs) [56]. From a radiobiological point of view, helium ions show a larger relative biological effectiveness (RBE) [57] and smaller oxygen enhancement ratio (OER) than protons for similar penetration depths in water. Additionally, helium ions undergo less multiple scattering than protons, leading to reduced distal and lateral beam straggling, and less projectile fragmentation than carbon ions, reducing the dose delivered in the distal part of the target volume. Several studies have been carried out investigating the possible advantages of treating cancer by combining helium ions with other particles, in order to exploit the radiobiological properties of different ions simultaneously [58, 59]. Additionally, helium ions have been identified as a good candidate for spatially fractionated therapy applications, such as mini-beam radiation therapy, due to their reduced multiple Coulomb scattering and reduced nuclear fragmentation with respect to protons and heavier ions [60]. Besides its direct application in therapy, helium is also very interesting for radiography applications, due to its favorable physical properties compared to protons [61]. Additionally, the possibility of directly mixing helium and carbon beams for direct online monitoring (helium) of the treatment (carbon) is currently being explored [62]. Based on the current interest in embracing helium as a viable alternative for proton and carbon beams, the following conclusion can be stated:

- The availability of high-quality ^{4}He cross section data for transport code optimization and validation in the energy region of interest for ion therapy ($<$ 220 MeV/n) is crucial for reestablishing helium as a safe alternative for proton and carbon treatments and to enable novel medical use cases.

2.3 Required Cross Section Measurements

Having discussed the importance of He projectiles for space radiation and ion therapy, the question of which reactions are necessary to meet requirements is now addressed. A variety of low to medium mass targets are needed as well as a range of projectile energies.

- Inclusive, isotopic, double differential cross sections should be measured for the complete set of neutron and light ion fragments,

$$^4\mathrm{He} + \mathrm{H, C, O, Al, Fe} \rightarrow \mathrm{n}, ^{1,2,3}\mathrm{H}, ^{3,4}\mathrm{He} + \mathrm{X} \tag{2}$$

for projectile kinetic energies ranging over 50 MeV/n–50 GeV/n and fragment angles ranging over 0°–180°.

3 PRESENT STATUS

3.1 Measurements

Section 1.3 discussed the availability of measurements for all types of projectiles. However, previous work [1–4] did not discuss the quality or usefulness of the measurements, and it will be seen below that when measurement quality is considered, there is an even more pressing need for a new set of cross section data. Another aspect that should be considered when the quality of a

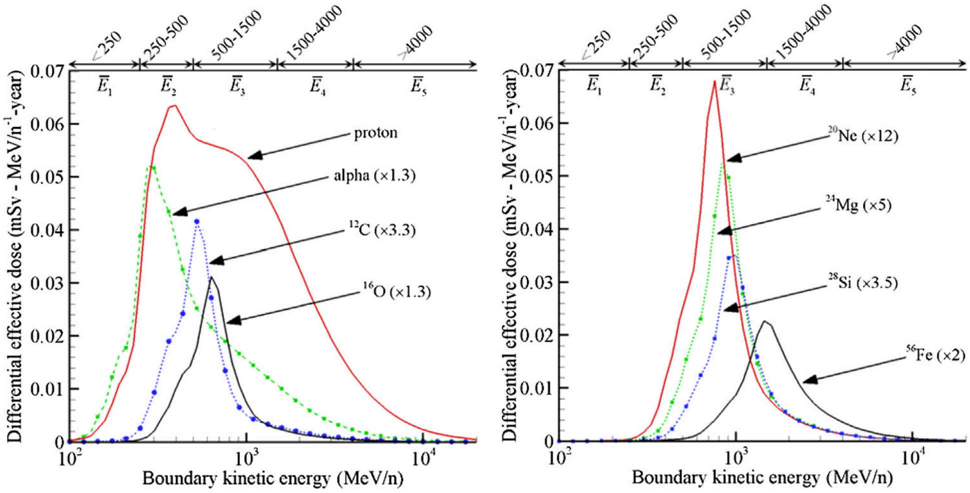

FIGURE 8 | Effective dose contributions as a function of external GCR energy behind 20 g/cm^2 of aluminum exposed to solar minimum GCR. Reprinted from Slaba and Blattnig [46].

TABLE 1 | Percent contribution of each energy range (MeV/n) to total He effective dose from external GCR spectrum for Al shield thicknesses of 20 g/cm^2 and 40 g/cm^2.

MeV/n	< 250 (%)	250 – 500 (%)	500 – 1,500 (%)	1,500 – 4,000 (%)	> 4000	
20 g/cm^2	10	18	34	24	14%	100%
40 g/cm^2	1	18	35	28	18%	100%

cross section dataset is evaluated is the target that was used for the measurement. Thinner targets give better data (better defined projectile kinetic energy, less elastic scattering, and less probability of multiple reactions) but increase the required beam time to collect data with appropriate statistical uncertainty. There is no universal definition what is a *thin* target. This should be judged based on the accuracy requirements for the measured cross sections as well as the ion species and energy used (see also **section 1.3.1**).

3.1.1 Total Cross Sections

Concerning total reaction cross sections for ^{4}He-induced reactions, there exists a quite comprehensive database, especially for light targets [42, 43, 63–80]. **Figure 12** shows an overview of this total cross section data set. Recently, measurements of charge- and mass-changing cross sections at therapeutic energies (70–220 MeV/n) were performed at HIT, Heidelberg, because for this energy range there were practically no data available in the literature [42, 43]. Accurate nuclear reaction models are required for precise dose calculations and treatment planning in ion therapy [53] and for transport code simulations of dose reduction in space shielding materials [81].

The energy range of the ^{4}He component in galactic cosmic radiation overlaps with the therapeutic energy range but also reaches up to very high energies. Therefore, ^{4}He nuclear interaction cross sections must be accurately modeled up to 50 GeV/n and above for radiation transport calculations related to space radiation. ^{4}He ions are also produced as secondaries through nuclear fragmentation of heavier ions of the GCR spectrum within the structural and shielding materials of a spacecraft. On the one hand, transport codes must consider the dose contribution from these secondary ^{4}He ions in human tissue (astronauts), and, on the other hand, their transport through shielding materials should also be calculated accurately. For these scenarios, ^{4}He reaction cross sections at lower energies become crucial.

The measurement of helium fragments produced from the fragmentation of heavier ions interacting with different target materials is important for nuclear models developed for space radiation transport models. NASA has specifically been interested in these data for validation of the nuclear fragmentation model NUCFRG. With this in mind, NASA collected experimental total cross sections, as NUCFRG only models the total cross section for production of isotopic fragments. This data gathering effort was restricted to projectiles with charge less than or equal to nickel. A total of 157 cross section values were found in the open literature at the time that work was performed [82–88]. The data are concentrated in the medium projectile energy range (280–3,000 MeV/n) with 135 cross sections. In the low projectile energy range ($<$ 280 MeV/n), there were 18 cross sections measured by 82, 83, while in the high projectile energy region (3–15 GeV/n), there were only three cross section measurements by 84 (and none for energies larger than 15 GeV/n). Interestingly, the data found only spanned projectiles between carbon (Z = 6) to magnesium (Z = 12). For model development and model

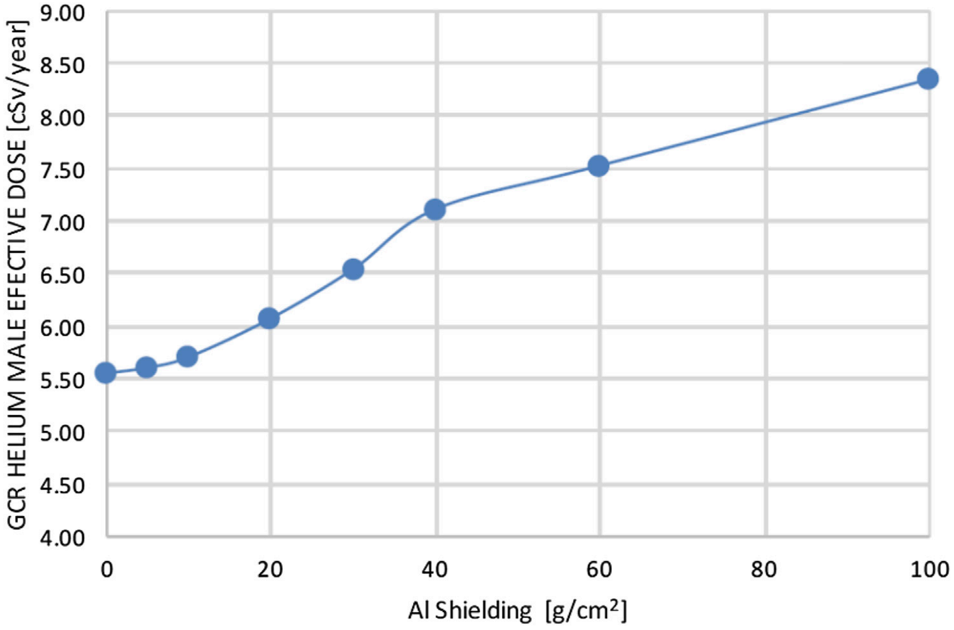

FIGURE 9 | Geant4 simulation of Male Effective dose due to GCR He (including its secondary particles), calculated using the ICRP Publication 123 fluence to dose conversion factors with NASA quality factors.

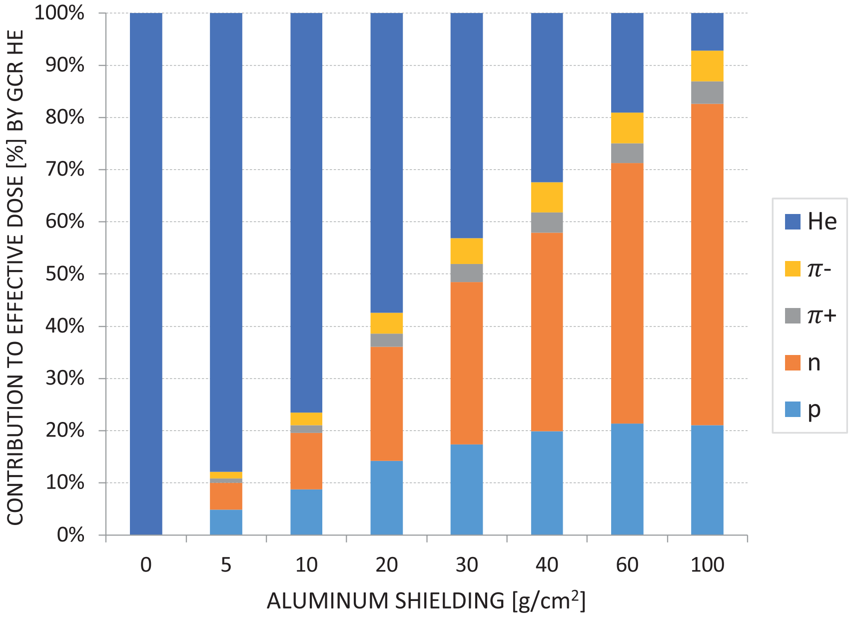

FIGURE 10 | Geant4 simulation of the percent contribution to the male effective dose of He GCR, showing in percentage the radiation component responsible for the GCR HE dose (either primary He or secondary particle generated by GCR He). Total male NASA effective dose has been calculated with ICRP Publication 123 fluence to dose conversion factors. 0 g/cm^2 refers to a free space scenario and applying the NASA quality factors.

validation purposes, this dataset is limited. Additional measurements at all projectile energies for projectiles with atomic number less than six and larger than 12 are desired. Also, more measurements are needed outside the medium energy range to better understand model development needs. For space research, He projectile measurements in the 0.2–3 GeV/n energy range should be prioritized, as indicated by the results in **Figure 11**.

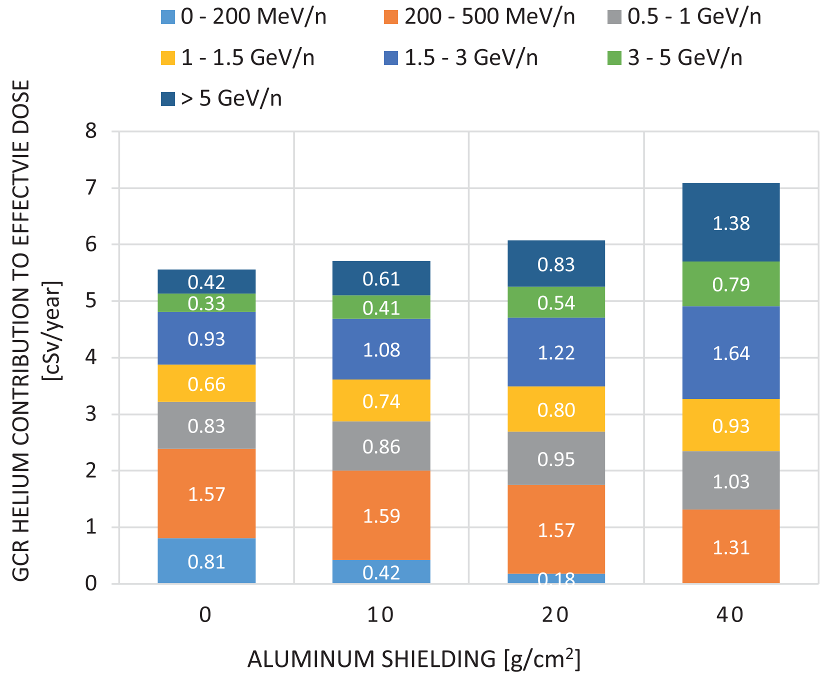

FIGURE 11 | GCR He energy ranges contributing to the 1 year NASA male effective dose for different thickness, using fluence to dose conversion factors from ICRP Publication 123.

3.1.2 Light Ion Fragment Production

Partial (Non-Differential) Cross Sections

Cross sections for ^{4}He fragmentation reactions on H, C, and O targets were recently collected for radiation transport modeling in ion therapy [31]. Within the framework of this data collection, only limited partial cross section data were found, some for ^{1}H targets [89] and some for ^{12}C targets [90]. In [91], the cross section for ^{1}H production by 27 MeV/n ^{4}He impinging on ^{165}Ho is reported.

Additional cross sections for ^{1}H, ^{2}H, ^{3}H, ^{3}He, and ^{4}He production by 400 MeV/n ^{4}He projectiles on U targets are presented in 92. Inclusive ^{3}He production cross sections can be obtained by subtracting ^{4}He charge- from mass-changing cross sections. This method has been used to calculate ^{3}He production cross section data for ^{4}He projectiles on ^{12}C, ^{16}O, and ^{28}Si targets [42, 43]. ^{3}He production cross sections for 630, 970, and 1,017 MeV/n ^{4}He projectiles impinging on H targets were reported by 70, 93, 94.

Differential cross sections

The available helium projectile double differential data are listed in **Table 2**. A high-quality data set is required, and therefore some data are not useful. For example, many data do not include error bars [92, 97], and other data have not been published in refereed journals. Also, many data are for proton fragments only [91, 96, 99]. In addition, many data sets measured only large angles or only very small angles. There are certainly no data sets covering all the requirements of the necessary reactions of **Eq. 2**. Given these problems, it is recommended that a new experimental program be initiated that covers all the reactions listed in **Eq. 2**. There might be a *small* amount of overlap with *some* of the reactions on **Table 2**, but that will serve as a very useful benchmark to check the accuracy of new measurements.

Some recent investigations in the scope of helium ion therapy [102, 103] provided experimental data about double differential fragment yields behind thick water and PMMA targets which can also be useful for nuclear model validation.

3.1.3 Neutron Production

From **Figure 10**, it is possible to see how the neutron contribution increases with spacecraft shielding thickness. From 104, discrepancies are found when comparing neutron ambient dose with PHITS and Geant4 simulations results. There is a need to have better models to simulate neutron production from space GCR.

Differential Cross Sections

There is a limited set of inclusive double differential cross-sectional data available on neutron production from medium and high energy ^{4}He ions, especially when compared to the amount of data available from He interactions in thick (stopping) targets. The last two rows of **Table 2** list the measurements taken and published to date. The quality of the data from the 135 MeV/n He systems [105] is very good due to the experimental setup at RIKEN that provides a low background environment for time-of-flight measurements, as well as the capability to measure neutrons at 0° relative to the beam axis. Neutrons below 10 MeV were not measured in those systems, however, in part to avoid contamination from background neutrons in the measurement. The measurements at 230 MeV/n [106] were taken at HIMAC and had a higher background

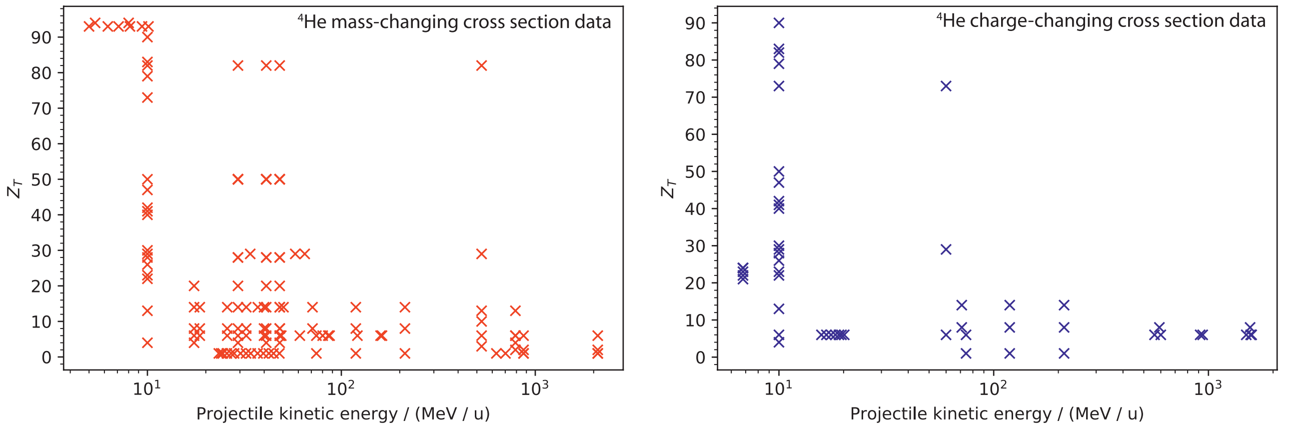

FIGURE 12 | Overview of ^{4}He experimental cross section data for different target atomic numbers Z_T as a function of kinetic energy for mass-changing **(left panel)** and charge-changing reactions **(right panel)**.

subtraction than the data taken at RIKEN. As a result, the 230 MeV/n double differential cross sections have fewer data points with larger error bars in each spectrum than the RIKEN data. The HIMAC data had lower neutron energy thresholds, however, extending the spectra down to three–5.5 MeV, depending on the angle of measurement. Measurements at 0° were not possible at HIMAC. In total, six systems were measured. The RIKEN measurements used C, Al, Cu, and Pb targets, and the HIMAC measurements used Al and Cu targets. All targets were composed of natural abundances of each element. There are good data from both systems at forward angles that characterize projectile fragmentation. For target fragmentation, measurements extend to 110°, yielding an incomplete picture of that process, especially given the relatively high neutron energy thresholds.

3.2 Modeling

While it is relatively easy to develop accurate models for total cross sections and more difficult to develop accurate single differential spectral or angular cross sections, it is most difficult to develop accurate double differential models. And again, charge changing or elemental production models are easiest, while isotopic models are the most difficult. Accurate isotopic double differential cross section models are the most difficult of all to develop, but once available, they automatically generate accurate total and single differential cross sections including charge-changing and elemental cross sections.

3.2.1 Applications in Ion Therapy and Space Radiation Research

Treatment planning systems (TPS) are standard applications in ion therapy. The first TPS for scanned ion beams was the GSI code TRiP98 [29, 107]. It has been used clinically in the carbon ion pilot project at GSI [53]. Special emphasis has not only been on dose calculation but also on dose optimization including radiobiological effects. It features a built-in deterministic transport model to create the base data necessary for treatment planning, that is, depth dose profiles and particle spectra which are necessary for radiobiological modeling. TRiP98 is now further developed as a research prototype for use with ion beams other than carbon, in particular oxygen [32] and helium [31]. TPS predictions have been validated in dosimetric and radiobiological experiments at HIT and KVI Groningen.

TRiP98 is a deterministic code based on a set of tables comprising single particle energy loss (dE/dx) for primary and secondary ions, nuclear reaction cross sections describing the loss of the primary ion beam, and fragmentation cross sections to compute the build up of the produced secondary ions. In this respect, it needs the same basic physics data as the various Monte Carlo codes. ^{4}He related cross sections are important in two ways. First, they are important for an accurate description of beam attenuation when ^{4}He is the primary beam. Second, they are also important to properly describe the "fragmentation tail" in case of heavier primary beams, since helium fragments are the second most abundant species after protons. ^{4}He cross sections are handled semi-empirically, as described in 31.

For space radiation research, TRiP98 is being extended to SpaceTRiP, in the framework of the ESA ROSSINI project. The latter is designed to calculate the dose reduction due to different space radiation shielding materials. The native TRiP98 transport model is extended to more types of ion projectiles than in ion therapy. This extension will allow the simulation of the multitude of HZE particles found in GCR spectra, of which ^{4}He is one of the most important ions.

Furthermore, the ^{4}He fragments are crucial for both ion therapy and space radiation due to the high penetration in various materials, compared to smaller penetration by heavier fragments. In ion therapy, He fragments can travel past the Bragg peak, which leads to undesirable dose to OARs, and in space radiation research, these fragments contribute significantly to dose buildup after the beam has traversed the shielding material.

TABLE 2 | He projectile double differential cross section measurement details. T_n is the kinetic energy of the outgoing neutron.

Projectile	Energy (MeV/n)	Target	Fragment	Author	Notes	Comments
^{3}He	33	Ho	^{1,2,3}H	Motobayashi [95]	17°–120°	**Figure 1**
^{3}He	67	Ag	^{1}H	Zhu [96]	> 33°	**Figure 1**
^{4}He	27	Ho	^{1}H	Shibata [91]	20°–140°	FIGURES 1 and **2**
^{4}He	180	Al,Ag,Ta	^{1,2,3}H,^{3,4}He	Doering [97]	> 60°	Often no error bars
^{4}He	383	C	^{1,2,3}H,^{3}He	Anderson [98]	0°	FIGURE 24, Unpublished
^{4}He	250	U	^{1,2,3}H,^{3,4}He	Gossett [92]	> 20°	**Figure 10**, No error bars
^{4}He	400	U	^{1}H	Westfall [99]	> 30°	**Figure 3**
^{4}He	400	U	^{1,2,3}H,^{3,4}He	Gossett [92]	> 20°	**Figure 10**, No error bars
^{4}He	400	U	^{1}H,Li, ^{7,9,10}Be,B	Gossett [92]	> 30°	**Figure 18**, No error bars Figure 26
^{4}He	400	C	^{1}H	Anderson [100]	0°	FIGURE 23 x_F axis
^{4}He	1,010	H	^{3}He	Bizard [93]	1°–10°	—
^{4}He	1,050	^{2}H,^{3,4}He	^{4}He	Banaigs [101]	< 15°	Elastic and inelastic
^{4}He	1,050	C	^{1}H	Anderson [100]	0°	**Figure 7**
^{4}He	1,050	C	^{4}He	Anderson [100]	$p^{\perp}$ axis	**Figure 10**
^{4}He	1,050	C	^{1,2,3}H,^{3}He	Anderson [100]	0°	**Figure 3**
^{4}He	1,050, 2,100	C	^{1}H	Anderson [100]	0°	FIGURE 23 x_F axis
^{4}He	1,050, 2,100	C	^{1,2,3}H,^{3}He	Anderson [98]	0°	FIGURES 25 and 26, Unpublished
^{4}He	1,050, 2,100	C	^{1}H	Anderson [100]	0°	FIGURE 21
^{4}He	2,100	C	^{1}H	Anderson [100]	$p^{\perp}$ axis	**Figure 8**
^{4}He	2,100	H,C,Cu,Pb	^{4}He	Anderson [100]	$p^{\perp}$ axis	**Figure 19**
^{4}He	2,100	C	^{1}H	Anderson [98]	$p^{\perp}$ axis	FIGURE 28, Unpublished
^{4}He	2,100	U	^{4}He	Gossett [92]	90°	**Figure 6**, No error bars
^{4}He	135	C,Al,Cu,Pb	n	Sato [105]	0°–110°	$T_n \geq$ 10 MeV
^{4}He	230	Al,Cu	n	Heilbronn [106]	5°–80°	$T_n \geq$ 3–5 MeV

3.2.2 Total Reaction Cross Sections

An important quantity for light and heavy ion transport codes is the total reaction cross section σ_R, which is typically obtained from a parameterization for the projectile–target combination and kinetic energy of interest. Most of these parameterizations are semi-empirical models that are fine-tuned to experimental cross sections.

Figure 13 shows a collection of total cross section data for ^{4}He-induced reactions [42, 43, 63–71] compared with two different parameterizations. It can be observed that the agreement of the models with the experimental data is better for light targets. Toward heavier targets, the deviations of the models from the experimental cross sections get larger, probably because the models have been optimized mostly for light target data. It is clear that for very light targets like H or He, the Tripathi parameterization for light systems [108], which was specifically optimized for those targets, is the one fitting the best for a broad range of energies, while the Shen parameterization fails in reproducing very low energy cross section data for H targets. For intermediate weight targets (from C to Si), the general parameterization by Tripathi et al. [109], with parameter optimizations described by Horst et al. [43], has been used for the left panel because it has been specifically optimized for targets in this atomic number range, while the Tripathi light system parameterization [108] is optimized for very light targets. For very heavy targets, on the other hand, the Shen parameterization [110, 111] seems to work better, especially at higher energies. Nevertheless, none of the parameterizations can accurately reproduce the cross section data for targets heavier than Si. More experimental data points at high energy for heavy targets could help to optimize the models.

The modified Hybrid Kurotama model [112] for proton + nucleus and nucleus + nucleus total reaction cross sections can handle complex targets containing different target nuclei with both natural and unnatural abundances, for projectile energies from below 5 MeV/n to well above 10 GeV/n, where limiting fragmentation occurs. The model is based on the Black Sphere (BS) cross section formula for proton + nucleus reactions and extended to nucleus + nucleus reactions. However, the BS model requires that the de Broglie wavelength of the proton is considerably smaller than the nuclear size, and the BS model therefore breaks down below around 100 MeV/n. In addition, the Coulomb repulsion causes resonance features and a sharp increase at energies below 100 MeV/n, at which an energy dependent transparency parameter and the influence of the Fermi motion and Coulomb effects should be included. To solve the limitations of the BS model at low energies and to create a general purpose total reaction cross section model which can also be used for reactions with projectile energies below around 100 MeV/n, the BS model has been connected to the parameterization developed by Tripathi et al. [108, 109, 113]. The Hybrid Kurotama model has been extensively benchmarked against experimental total reaction cross section data, and an overall better agreement has been found than for earlier published models. The model is used in the PHITS transport code [17].

3.2.3 Partial (Non-Differential) Cross Sections

In addition to total reaction cross sections, models for partial (elemental and isotopic) cross sections are also required for calculation of the production of different fragment species. ^{4}He fragmentation reactions occur *via* a remarkably small number of channels where the only products are ^{3}He, ^{3}H, ^{2}H, ^{1}H, and neutrons. This allows for individual modeling of all reaction channels. **Figure 14** shows model predictions for the

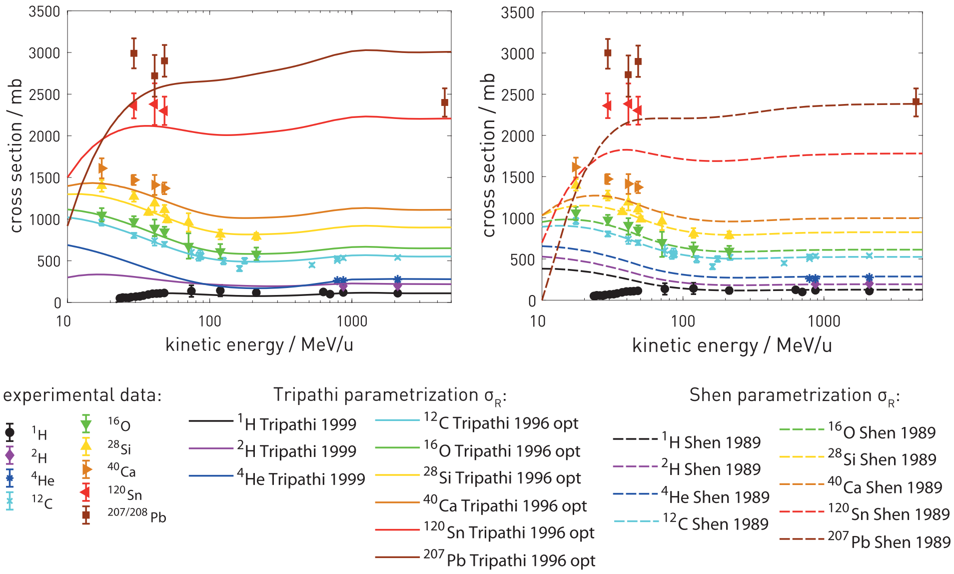

FIGURE 13 | Experimental data of total cross sections for ^{4}He-induced reactions on different targets, whose atomic numbers range from low (^{1}H) to high (^{207}Pb), compared with two different parameterizations. In the left panel the predictions by the Tripathi parameterization of the total reaction cross section are shown. The light system model by Tripathi et al. [108] is used for low atomic number targets (^{1}H, ^{2}H, and ^{4}He) and the general model by Tripathi et al. [109] with the modifications described by Horst et al. [43] is used for higher atomic number targets. In the right panel, the predictions by the model by Shen et al. [110] with the modifications proposed by Sihver et al. [111] are shown. The experimental data were taken from 42, 43, 63–71.

total reaction cross section and the inclusive ^{3}He production cross section compared with data.

The total reaction cross section model shown in **Figure 14** is the parameterization by Tripathi et al. [109], and modified by Horst et al. [42, 43], based on recent experimental cross sections. These modifications result in a significant improvement of the agreement between calculated and measured ^{4}He Bragg curves in water, which are important for ion therapy applications [33, 115].

^{3}He production is the only channel that can occur for ^{4}He projectiles which changes the mass but not the charge. Therefore, the ^{3}He production cross section can be obtained by subtracting experimental cross sections for charge-changing reactions from those for mass-changing reactions. This is how the red symbols in **Figure 14** were obtained. A semi-empirical model for inclusive ^{3}He production in ^{4}He-nucleus collisions was developed by Cucinotta et al. [114]. This model accounts for break-up of the ^{4}He projectile into ^{3}He and a neutron, as well as for the decay into ^{3}He and ^{2}H after proton pickup. A scaling with $A_T^{1/3}$, where A_T is the mass number of the target, which corresponds to the radius of the target nucleus, has been proposed in order to use the model for heavier targets, because neutron stripping was assumed to occur mostly in surface reactions. However, it was found empirically, by comparison of model predictions with the recent experimental data, that a $A_T^{2/3}$ scaling, corresponding to the geometrical cross section of the target nucleus, better describes the dependence of ^{3}He production on the target material. In addition to the replacement of the target mass number scaling, also a downscaling of the parameterization by a factor of 0.85 is proposed for an optimal fit of the model to the experimental data. As demonstrated in **Figure 14**, the agreement between the predictions of those two optimized models with the experimental cross section data for ^{12}C, ^{16}O, and ^{28}Si targets is reasonable.

3.2.4 Double Differential Cross Sections

Heavy ion production isotopic double differential cross sections can be modeled with relatively simple physical ideas because the ions are mostly produced from simple abrasion–ablation processes, and because the ions are heavy, they proceed mostly in the forward direction. The abrasion–ablation model [116] assumes that the dominant source of heavy ion production is from the incident projectile. On the other hand, neutron, proton, and composite light ions are scattered at large angles because they are relatively light. Also, composite light ions have a complicated production mechanism, often involving not only abrasion–ablation but also coalescence.

The general picture for high-energy heavy ion projectile collisions is the following: The projectile and target nuclei collide and form a central fireball overlap region, together with deformed and excited projectile and target pre-fragments, which decay into lighter fragments. The fireball is very hot and decays quickly with the emission of pions, other mesons, and baryons such as neutrons, protons, and other particles. The cooler excited projectile and target pre-fragments decay more slowly, generally by emitting nucleons, which may coalesce into light ions. There are therefore three different sources of particles, the projectile and target pre-fragments and the central fireball. Each of these three sources can produce the same type of particle that eventually reaches detectors in the lab frame (or an astronaut's body in a spacecraft). Because the fireball is very hot, light ion

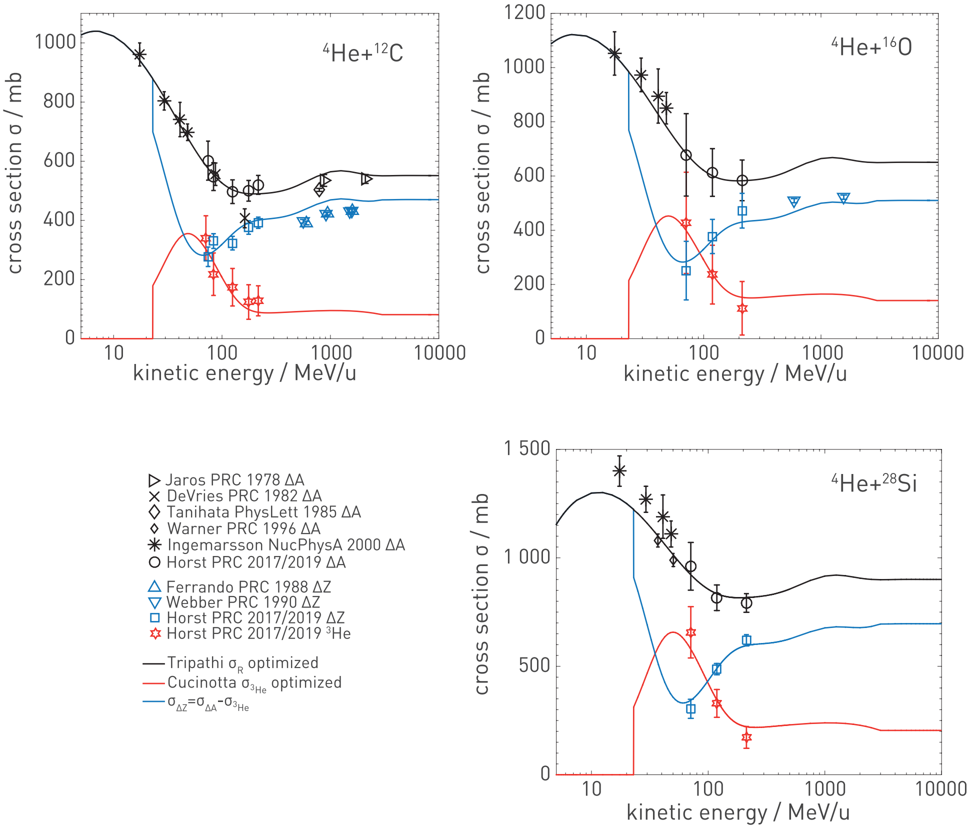

FIGURE 14 | ^{4}He nuclear fragmentation models compared with experimental cross sections. Black symbols: mass-changing *ΔA*, blue symbols: charge-changing *ΔZ*, red symbols: inclusive ^{3}He production. Cross sections are obtained by subtracting the charge- from the mass-changing experimental cross sections. The black line shows the Tripathi model of the total reaction cross section [109] with optimized parameters described in 43. The red line shows a model designed by Cucinotta et al. [114], optimized according to the description in the text. The blue line shows the charge-changing cross section calculated by subtracting red from black. The plotted experimental data are from 42, 43, 63–66, 68.

fragments cannot survive and will be broken up into baryons and mesons. However, what happens when the fireball cools? The answer is similar to what happened in the very early Universe. After a rapid period of inflation, the Universe started as a quark-gluon plasma, which then cooled and formed hadrons such as pions, kaons, other mesons, nucleons, deltas, and other baryons. After further cooling the baryons decayed to nucleons, which later *coalesced* into light ions: H, He, and some Li. Then, the density dropped too rapidly to form heavier ions, which were made much later in stellar interiors, supernovae [117], and binary neutron star mergers [118]. As the Universe cooled further, electrons and light ions coalesced into atoms. Aspects of the nuclear fireball cooling are similar to the early Universe scenario. As the fireball cools and decays and emits neutrons and protons, these are cool enough to coalesce into the light ion isotopes of H and He (and also some Li). As with the early Universe, the fireball density drops very rapidly, and nucleons are unable to coalesce to form heavier ions, which come from projectile and target pre-fragments. Of course, the projectile and target pre-fragments also emit nucleons (neutrons and protons), and these can also coalesce. Thus, light ions are produced from nucleon coalescence [12, 13, 119] of all three sources: projectile, fireball, and target. This is in contrast to the simpler mechanism of abrasion–ablation of heavy ions, where the dominant source is the incident projectile. Another complicating factor for neutron, proton, and composite light ion production is that there are two production mechanisms from each of the three sources, namely, direct production vs. thermal emission of nucleons with subsequent coalescence.

Despite all these complications, models for neutron, proton, and composite light ion production have been recently developed [12, 13, 119, 120] and compared to a variety of data. DDFRG is a double differential fragmentation model based on Lorentzian parameterizations of the projectile, fireball, and target sources including direct and thermal/coalescence production. Results for helium projectiles producing fragments at 0° are shown in **Figure 15**, and compared to the cross section models used in the SHIELD transport code, which incorporates nuclear models that include both the internuclear and intranuclear processes in matter. Inelastic nuclear reactions present the following sequential stages of the whole interaction: fast intranuclear cascade, coalescence of the cascade nucleons, possible pre-equilibrium decay of residual nuclei, and the equilibrium de-excitation of the residual nuclei. The last includes the advances evaporation, fission, multifragmentation (for large residues), and Fermi-Breakup (for light residues) processes. All of these models have a good performance in description of experiment [121–128]. **Figure 15** shows that proton, triton (^{3}H), and helion (^{3}He) production is described well with both DDFRG and SHIELD models. Deuteron production data are not as well described by the SHIELD models, and presents somewhat of a puzzle. DDFRG describes the data quite well only because several parameters have been tuned to the data. The production of ^{3}H and ^{3}He is described in the SHIELD models due to stripping of a single nucleon, rather than coalescence production, which is why SHIELD results for deuteron (^{2}H) production give much smaller values than ^{3}H and ^{3}He production. There is therefore an urgent need for the following:

- Experimental double differential cross section results [100] for light ion production from He projectiles need to be confirmed, including angles 0°–180°.
- SHIELD double differential cross section results for light ion production from He projectiles need to be confirmed by comparing to other cross section models.

Other approaches to nuclear cross section modeling are under development. A deterministic Serber nuclear model was developed for use in the radiation transport code, HZETRN, with the aim of improving nucleon spectral and angular distributions. Various implementations of the Serber nuclear models have been employed successfully in Monte Carlo codes for internuclear cascade processes. The underlying theory describes the propagation of an incident nucleon through target media modeled with a characteristic density and potential well. The target nucleus is composed of nucleons that are bound within a Fermi sea. When a projectile nucleon strikes a target nucleon, the kinetic energy of the struck nucleon must exceed the Fermi energy to escape the target. Both the spectra of the projectile nucleon and the recoil nucleons are tracked. The primary nucleon is assumed to traverse in the straight-forward direction, whereas the recoil spectra are assumed to have an angular dependence [129]. This model is being extended to nucleus–nucleus reactions for the evaluation of nucleon double differential and spectral distributions. Primary nucleons and nucleons resulting from internuclear processes, including abrasion and de-excitation, are among the most consequential reactions for the projection of radiation risk. Additional nucleon and light ion fragmentation data for space radiation relevant reactions are needed to validate the nuclear models. The current process of validating models (when data are not available) is to compare transport code results in thin target simulations, which ultimately is a comparison of the different cross section models. Ideally, the nuclear cross section models would be compared directly to nuclear data, but additional experiments are needed to support these efforts and is the subject of the current work.

4 REVIEW OF ACCELERATORS

The aim of this section is to summarize the availability of accelerators for helium ion beams. The ideal accelerator facility for the intended cross section measurements would provide helium ions in an energy range from typically 50 MeV/n up to 50 GeV/n. These conditions can only be met by large-scale research facilities like GSI/FAIR, the Joint Institute for Nuclear Research (JINR, Dubna), and the NASA Space Radiation Laboratory (NSRL) at Brookhaven National Laboratory (BNL). However, since beam time at these accelerators is relatively expensive and has to be planned on a long time scale, it might be convenient to supplement the use of high-energy accelerators with medium-energy accelerators, which are more readily available. Especially, medical facilities often provide experimental beam during the night after finishing quality assurance. Thus, medium to high energies (100–800 MeV/n) could be delivered by some medical facilities for ion beam therapy like the HIMAC accelerator in Chiba or the HIT facility in Heidelberg. In some cases, low-energy facilities, such as the KVI in Groningen, could be a cost effective addition for the helium cross-section measurement program. However, in order to meet the requirements for space radiation research and ion beam therapy, a minimum energy of 50 MeV/n is specified that should be reached by the accelerator. This limit defines a subset of existing accelerators that will be presented for this study. **Table 3** comprises the eligible accelerators corresponding to the above mentioned requirements.

GSI/FAIR. GSI Helmholtzzentrum für Schwerionenforschung plays a special role among the facilities listed in **Table 3** because it fulfills all requirements for a comprehensive cross section measurement program. During FAIR-phase-0, the current project phase until completion of the SIS100 synchrotron cross section, experiments can be conducted at different irradiation sites with different profiles. Cave M and Cave A, which are used by the GSI biophysics group, can accommodate compact experiments such as the FOOT [130] experiment. Cave C provides space for experiments with larger detectors [131], while the fragment separator (FRS) [132] allows high precision charge-changing cross-section and double differential measurements at small angles ($<1^\circ$). The GSI control system allows very flexible settings for the beam intensity (100–10^9 ions/s), different extraction modalities, and spill extraction duration times (<1 ms up to 10 s and more). After commissioning of the SIS100 synchrotron, helium cross sections can be measured additionally at very high energies (E <10 GeV/n), relevant for space radiation research. A suitable irradiation site will be at the BIOMAT beamline in the APPA Cave [133].

NSRL/BNL. NSRL is a multidisciplinary center for space radiation research funded by NASA and located at the Brookhaven National Laboratory (BNL). Operational since 2003, the scope of NSRL is to provide ion beams in support of NASA programs in radiobiology, physics, and engineering [134]. Recently, it has also been recognized as the only facility in the United States currently capable of contributing to heavy ion therapy research. The facility provides a large room (10 m long from exit window to beam dump), well suited for time of flight (TOF) and double differential cross section measurements [135].

Nuclotron. The Dubna Nuclotron was the world's first superconducting synchrotron, built by the Joint Institute

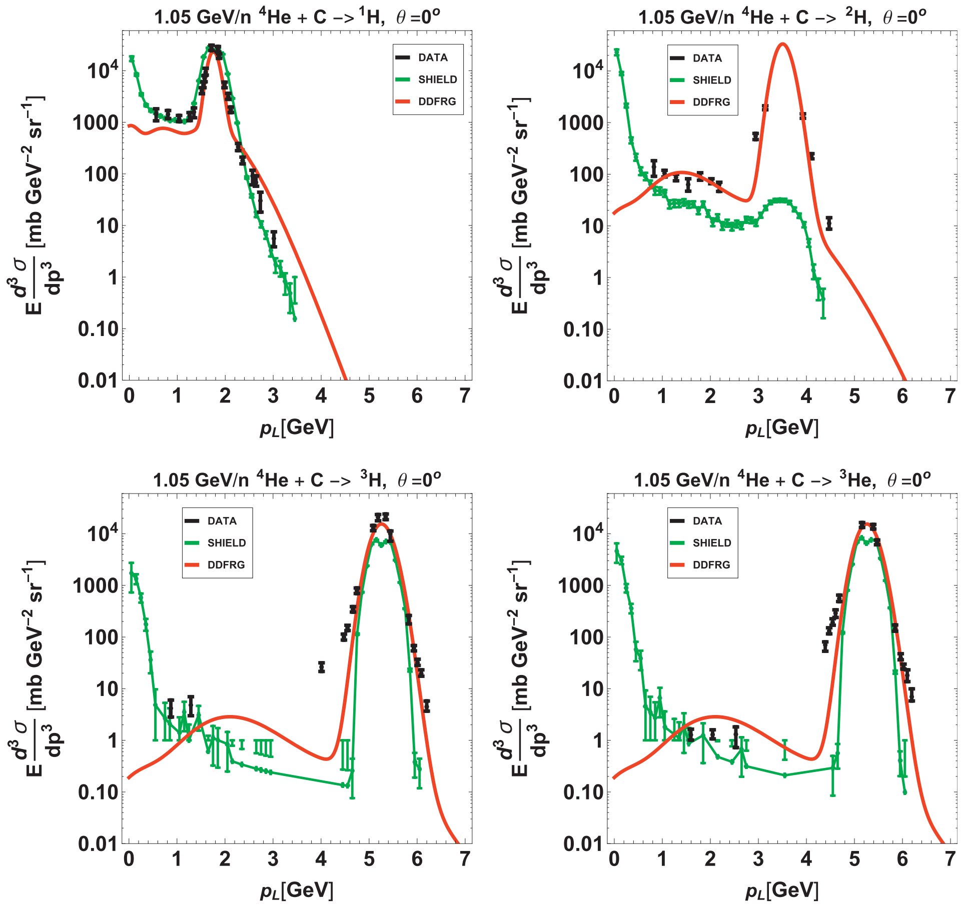

FIGURE 15 | Lorentz-invariant double differential cross section data [100] compared to DDFRG [119] and nuclear physics models from the SHIELD transport code [121–128].

for Nuclear Research (JINR), Russia. In the past, the accelerator was used to extract ion beams with Z = 1–36 up to energies of 2.2 GeV/n. As part of the upgrade for the NICA project [136], the beam energy can be increased up to 4.5 GeV/n in future. The nuclotron facility comprises various large experimental rooms and would enable the full spectrum of cross section measurements with helium beams.

Clinical facilities: HIT, HIMAC, MedAustron, and CNAO. Clinical facilities with medium to high energy can complement the measurements at the large-scale research facilities and can decrease the costs and effort for the whole cross section program. The Heavy Ion Medial Accelerator in Chiba (HIMAC) in Japan is part of the National Institute of Radiological Sciences (NIRS) and has been operational since 1993 as a medical facility for treating cancer patient with protons and carbon ions. The center has also served as a multi-user facility for medical, biological, and physics research. It can accelerate all ions between ^{4}He - ^{20}Ne up to 800 MeV/n. The HIMAC provides beam lines and experimental rooms to allow cross section measurements with helium beams [137]. The same applies for the Heidelberg Ion-Beam Therapy Center (HIT) facility. HIT intends to start the clinical treatment of cancer patients with helium ions at the end of 2020. This will be the first resumption of helium ion therapy worldwide after a long time. HIT provides a well-equipped experimental room, which has been used intensively in the past for helium cross section measurements [42, 43] and provides energies up to 430 MeV/n. The Centro Nazionale di Adroterapia Oncologica (CNAO) medical facility for ion beam therapy in Italy also accommodates an experimental room which meets the conditions for cross-section experiments [138]. The CNAO is updating their accelerator for a helium ECR source and intends to deliver ^{4}He beams up to 330 MeV/n from the beginning of 2021. The MedAustron ion-beam therapy facility in Wiener Neustadt (Austria) [139] also has the hardware available to accelerate helium ions up to 400 MeV/n. However, a commissioning for helium beam will not take place before 2023.

AGOR/KVI-CART and LNS. In case of difficulty obtaining helium beams at large-scale and medical facilities, the AGOR cyclotron facility (KVI-Centre, Groningen) could provide ^{4}He beams for energies ≤ 90 MeV/n (≤ 120 MeV/n for ^{3}He). Similar ^{4}He beams, but at slightly lower energies (62 and 80 MeV/n), can

TABLE 3 | Suitable accelerator facilities for helium cross-section measurements.

Facility name **Location/country**	**Ion**	**Energy range**
Existing facilities		
GSI/FAIR		
Darmstadt/Germany	^{1}H	E = 70–4,500 MeV
SIS18 synchrotron	^{3}**He** - ^{20}N	**E = 70–2,000 MeV/u**
BNL/NSRL		
Brookhaven/United States	^{4}**He** - ^{56}Fe	**E ≤ 1,500 MeV/u**
AGS Booster, synchrotron		
JINR		
Dubna/Russia	^{4}**He** - ^{56}Fe	**E ≤ 2,200 MeV/u**
Nuclotron supercond. synchrotron		
NIRS/HIMAC		
Chiba/Japan	^{4}**He** - ^{20}Ne	**E = 50–800 MeV/u**
Synchrotron		
HIT		
Heidelberg/Germany	^{1}H	E = 50–480 MeV/u
compact synchrotron	^{4}**He** - ^{16}O	**E = 100–430 MeV/u**
AGOR/KVI-CART	^{1}H	E ≤ 190 MeV
Groningen/Netherlands	^{3}**He**	**E ≤ 120 MeV/u**
supercond. cyclotron	^{4}**He**, ^{12}C, ^{16}O	**E ≤ 90 MeV/u**
K800/LNS		
Catania/Italy	^{2}H, ^{4}**He**, ^{12}C, ^{16}O	**E = 62 and 80 MeV/u**
supercond. cyclotron		
Future facilities		
GSI/FAIR		
Darmstadt/Germany	^{1}H	E ≤ 29 GeV/u (not before 2025)
SIS100 supercond. synchrotron	^{4}**He** - ^{20}N	**E ≤ 14 GeV/u** (not before 2025)
JINR/NICA		
Dubna/Russia	^{4}**He** - ^{56}Fe	**E ≤ 4.5 GeV/u** (not before 2020)
Nuclotron (upgr.) supercond. synchrotron		
MedAustron	^{1}H	E ≤ 800 MeV (available)
Wiener Neustadt/Austria	^{12}C	E ≤ 400 MeV/u (available)
Synchrotron	^{4}**He**	**E ≤ 400 MeV/u** (not before 2023)
CNAO		
Pavia/Italy	^{1}H	E = 63–230 MeV (available)
compact synchrotron	^{12}C	E = 115–400 MeV/u (available)
to be upgraded for He	^{4}**He**, ^{7}Li, ^{16}O	**E = 115–330 MeV/u** (not before 2023)

be provided by the superconducting K800 cyclotron at the INFN Southern National Laboratory (LNS) in Catania.

5 FOOT PROGRAM

5.1 Description of Program

FOOT (FragmentatiOn Of Target) [140–142] is an experiment funded by the INFN (Istituto Nazionale di Fisica Nucleare, Italy), aiming at the measurement of double differential cross sections for the production of charged particles in nuclear fragmentation which are of interest for medicine (hadron therapy) and radioprotection in space missions. The experiment has been originally designed with the main goal of investigating target fragmentation in proton therapy by means of an inverse kinematic approach, using beams of ^{12}C, and ^{16}O on graphite and polyethylene targets, to extract cross sections for the production of charged fragments in p+C and p+O collisions. The inverse kinematic approach is needed because the target fragments produced by proton beams would have too short ranges in matter (tens of microns), preventing the possibility of a direct measurement. However, it is straightforward for the same apparatus to investigate the fragmentation cross section in the direct processes C+H, C+C, O+H, and O+C. Using different target materials, like PMMA, also the collisions with other nuclei of interest for biological effects, like oxygen, can be studied. One can also consider possible direct kinematics measurements, and primaries other than C and O. The case of ^{4}He has been recognized as one of the main priorities. The energy range of nuclear projectiles under consideration by FOOT spans from 100 to 200 MeV/n, useful for the applications to hadron therapy (and proton therapy in particular), up to 700–800 MeV/n for the investigation of direct kinematics reactions relevant for space radioprotection. A summary of the physics program of FOOT is reported in **Table 4**.

The accuracy goal of FOOT is to identify charge and mass of the produced fragments with an accuracy of 3% and 5%, respectively, and to measure their energy spectra with a resolution of 2 MeV. Taking into account these goals, the idea is to realize a "portable" experimental setup in order to operate it in different facilities and to have some flexibility to optimize its configuration for different energy ranges. The detector design has been guided by Monte Carlo simulations, based on the FLUKA code [143, 144]. It shows that in the whole energy range under consideration, light ($Z \leq 3$) fragments have a wide emission angle, while the heavier fragments are forward peaked within a narrow cone: a semi-aperture of $\theta \sim 10^\circ$ ensures sufficient containment. In order to give an idea of energy and angle distribution of secondary fragments in ^{4}He interactions, the differential cross sections, in energy and angle have been considered for different fragments at the projectile energy of 700 MeV/n, as predicted by the FLUKA code. In **Figure 16**, dσ/dE is shown for three different targets (H, C, and O) integrated in the forward hemisphere ($0^\circ \leq \theta < 90^\circ$), while dσ/dΩ is given in **Figure 17**.

On the basis of the experimental goals summarized above, the FOOT experiment has been conceived considering two complementary experimental configurations:

(1) An electronic configuration based on a magnetic spectrometer dedicated to the momentum reconstruction and an identification section made of a plastic scintillator and a calorimeter. This setup aims to measure fragments heavier than ^{4}He ($Z \geq 3$) and covering a polar angle of $\theta \pm 10^\circ$ with respect to the beam axis;
(2) A configuration based on an emulsion spectrometer supplying complementary measurements for light fragments emitted at an angle up to about 70°.

This approach of employing two complementary detection techniques is particularly useful in the measurement of ^{4}He interactions, with only $Z \leq 2$ fragments; the angular acceptance of the emulsion setup allows one to cover a large part of the necessary phase space, and a cross-check in the acceptance cone of the electronic detector allows a cross-check of results and a control of possible systematics. A sketch of the electronic detector is shown in **Figure 18**, and fragment momentum, kinetic energy, time of flight (TOF), and energy loss (dE/dx) are measured. The detector geometry consists of the following:

(1) Upstream/target region: A thin plastic scintillator counter provides the start signal of the TOF and the trigger system, and downstream, a drift chamber operates as a beam monitor, tracking the direction and the position of the beam. The target is positioned beyond the beam monitor.
(2) Magnetic region: It is composed of three stations of pixel and strip detectors allocated between and downstream of the magnets providing the vertex reconstruction and the initial tracking of the produced fragments; two permanent dipole magnets supply the magnetic field (up to 1.4 T).
(3) Identification region: It is the distal part of the detector, located at least 1 m away from the target (more for higher energies). It is composed of two orthogonal planes of plastic scintillator rods, providing the stop of the TOF and the measurement of the energy loss. A BGO calorimeter provides the fragment kinetic energy measurements.

TABLE 4 | FOOT research program.

Physics	Beam	Target	Energy	Kinematic
–	–	–	(MeV/n)	Approach
Target fragmentation in proton therapy	^{12}C	C, C_2H_4	200	Inverse
Target fragmentation in proton therapy	^{16}O	C, C_2H_4	200	Inverse
Beam fragmentation in proton therapy	^{4}He	C, C_2H_4, PMMA	250	Direct
Beam fragmentation in proton therapy	^{12}C	C, C_2H_4, PMMA	350	Direct
Beam fragmentation in proton therapy	^{16}O	C, C_2H_4, PMMA	400	Direct
Space radioprotection	^{4}He	C, C_2H_4, PMMA	700	Direct
Space radioprotection	^{12}C	C, C_2H., PMMA	700	Direct
Space radioprotection	^{16}O	C, C_2H_4, PMMA	700	Direct

The TOF, measured by the start counter and the scintillator, has an estimated resolution at the level of 70–100 ps. The silicon detectors, in the magnetic region, are able to perform momentum measurements with an expected resolution of about 5%, while the resolution supplied by the scintillator and by the calorimeter is about 3 and 2%, respectively, in the measurement of the energy loss and kinetic energy. The emulsion spectrometer is built using Emulsion Cloud Chamber (ECC) technology, alternating nuclear emulsion films with passive material [145]. A sketch of the ECC is shown in **Figure 19**.

The ECC acts as a micrometric tracking device, ionization chamber, and a spectrometer for isotope separation. The nuclear emulsion films consist of two 50-μm thick sensitive emulsion layers deposited on both sides of a plastic base, 200 μm thick, resulting in a total thickness of 300 μm. AgBr crystals, dispersed in a gelatine matrix, are sensitive to ionizing particles and record their trajectory acting as latent image centers. A chemical process of development produces the latent image as silver grains recorded as dark pixels by an optical microscope. A dedicated software recognizes aligned clusters of dark pixels producing a track related to the path of the charged particle. The present design of the experiment does not allow for an efficient measurement of neutron production, which however is considered a relevant issue in radioprotection for space missions. Different ideas to extend the capability of FOOT to neutron detection are under study.

5.2 Present Status of the Experiment

Data have been taken using the ECC setup at GSI, in 2019 with O ions at 200 and 400 MeV/n on C and C_2H_4 targets, and in 2020 with ^{12}C ions at 700 MeV/n, on the same targets. Data analysis is still in progress. The electronic apparatus is under construction, and first data taking in this configuration are being scheduled at CNAO, using ^{12}C ions at 200 MeV/n. An application for beam

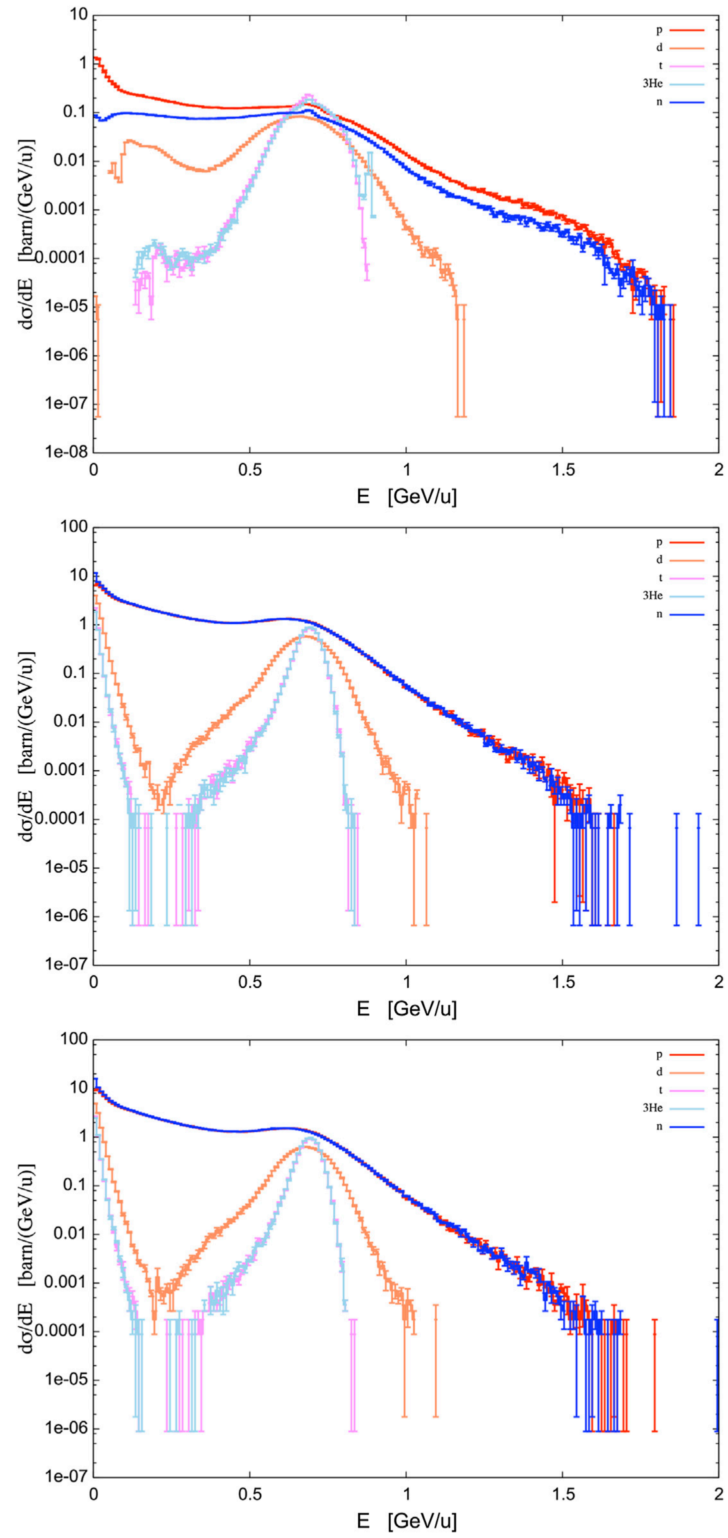

FIGURE 16 | Cross section differential in energy, integrated in the forward hemisphere, for inclusive production of secondaries of ^{4}He ions at 700 MeV/n impinging on different targets, as predicted by the FLUKA code. Three different targets have been considered: H **(top)**, C **(middle)**, and O **(bottom)**. Red: protons, blue: neutrons, orange: deuterons, violet: tritons, and sky blue: ^{3}He.

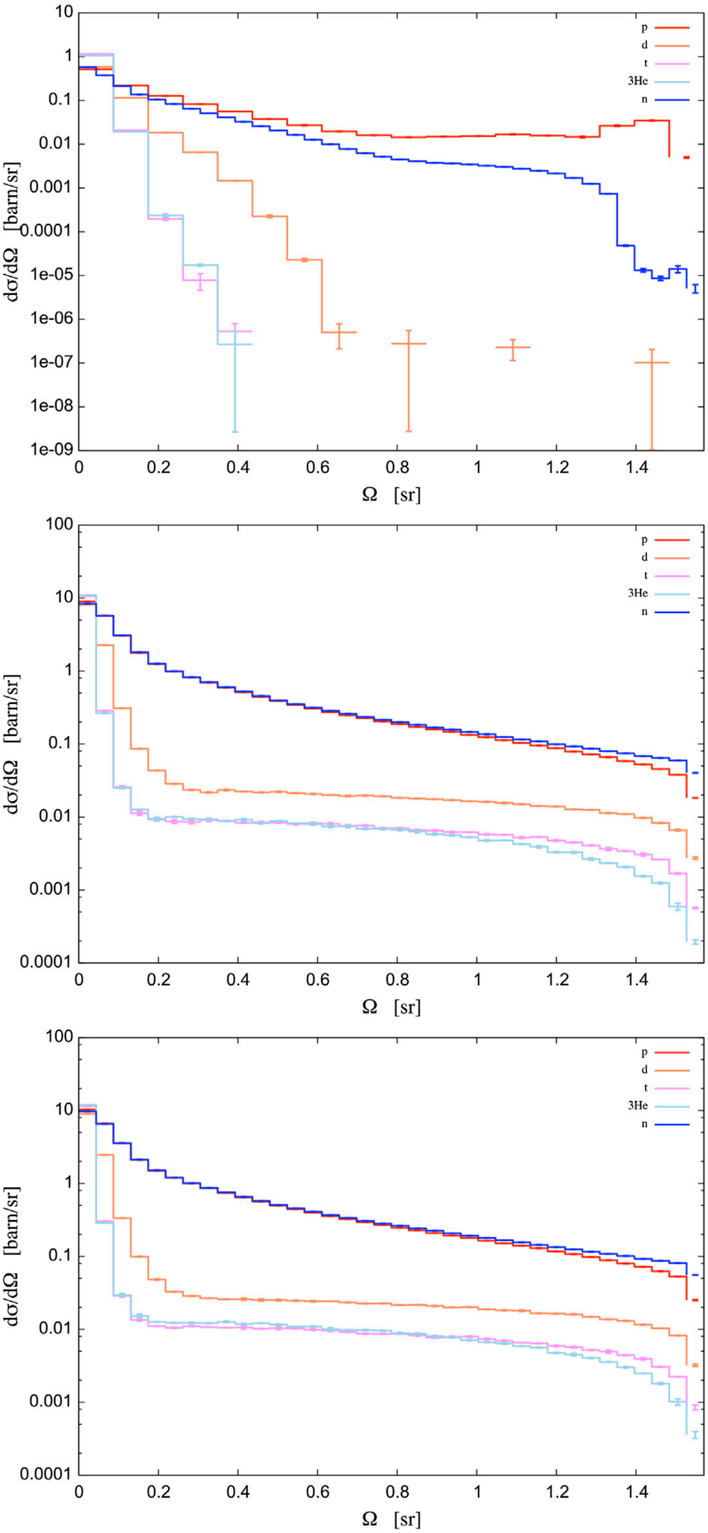

FIGURE 17 | Cross section differential in solid angle (forward hemisphere), integrated in energy, for inclusive production of secondaries of ^{4}He ions at 700 MeV/n impinging on different targets, as predicted by the FLUKA code. Three different targets have been considered: H **(top)**, C **(middle)**, and O **(bottom)**. Red: protons, blue: neutrons, orange: deuterons, violet: tritons, and sky blue: ^{3}He.

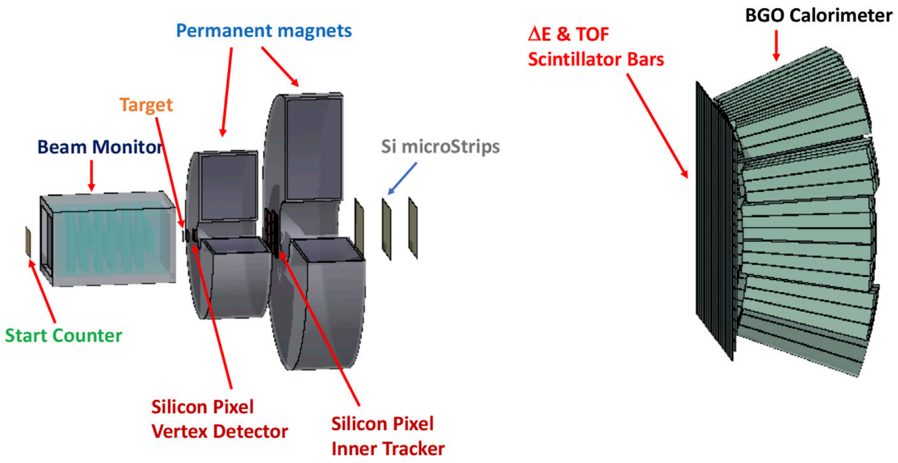

FIGURE 18 | Pictorial view of the FOOT electronic apparatus as obtained from the FLUKA graphical interface.

time in 2021/2022 at GSI is in preparation, having as one of the main priorities the request of a ^{4}He ion beam at 700 MeV/n.

6 FUTURE RECOMMENDATIONS

6.1 Measurements

6.1.1 Total Reaction Cross Sections

Total reaction cross section data for ^{4}He projectiles on heavy targets are missing, especially for elemental targets heavier than oxygen at high energies (see **Figures 12** and **13**). The semi-empirical models match the existing data only roughly and more experimental data points are required in order to improve the models. These types of data are particularly interesting in the framework of simulating the propagation of GCR through spacecraft structural and shielding materials, whose atomic number can be high. The human body is also rich in high atomic number atoms, for example, Ca in the bones, as well as in different implants, for example, amalgam in the teeth and titanium implants in hips and bones, which makes such experimental data interesting for ion therapy as well.

Very low energy data are missing. They are important for modeling the energy dependence of the cross sections below and at the Coulomb barrier, which seems to be shifted toward to high energies for very heavy targets in the currently used parameterizations (see **Figure 20**). An appropriate modeling of the Coulomb barrier is important to accurately predict nuclear reaction thresholds.

6.1.2 Light Ion Production

Given the sparseness of the present data set and the need for a uniform set of data covering all energies appropriate to ion therapy and space radiation, new set of inclusive, isotopic, double differential cross sections should be measured for a complete set of neutron and light ion fragments for the reactions ^{4}He + H, C, O, Al, Ca, Fe $\rightarrow$ n, ^{1,2,3}H, ^{3,4}He + X for projectile kinetic energies ranging over 50 MeV/n–50 GeV/n and fragment angles ranging over 0°–180°.

6.1.3 Neutron Production

Given the limited set of direct measurements taken to date, there are a number of recommendations for additional neutron production data. Data are needed for He energies above 230 MeV/n, at all angles, especially angles beyond the existing measurements at 110°, and for neutron energies down to 1 MeV. Data are needed for hydrogen, nitrogen, and oxygen targets (tissue constituents), in addition to a range of solid targets used in previous experiments. Investigations of neutron production from He targets may be able to produce useful data through the use of inverse kinematics. For example, translation of data from the ^{4}He (p,n)X system to the ^{1}H(^{4}He,n)X system can yield information on production from hydrogen targets, which are difficult to implement in the laboratory.

6.2 Modeling

The ultimate use of new cross section measurements is the development of accurate theoretical cross section models that can be used in modern transport codes. As mentioned previously in the text, isotopic production double differential cross section will give more detailed information about the nuclear reactions, so measurements of these cross sections are important to verify the theoretical models. Some models have been developed previously, but often they are compared to only a limited data set. Ion therapy and space radiation applications require models to be accurate for a wide range of projectiles, energies, and targets. Therefore, a cross section modeling program proceeding in parallel with the measurement program needs to be initiated. The cross section models should be compared to *all* available cross section data, including previously measured total and single differential cross sections.

A special emphasis will be given to modeling the high energy ^{4}He beams. This can be achieved when experimental cross section data for ^{4}He projectiles with high energy (~ 10 GeV/n) will be

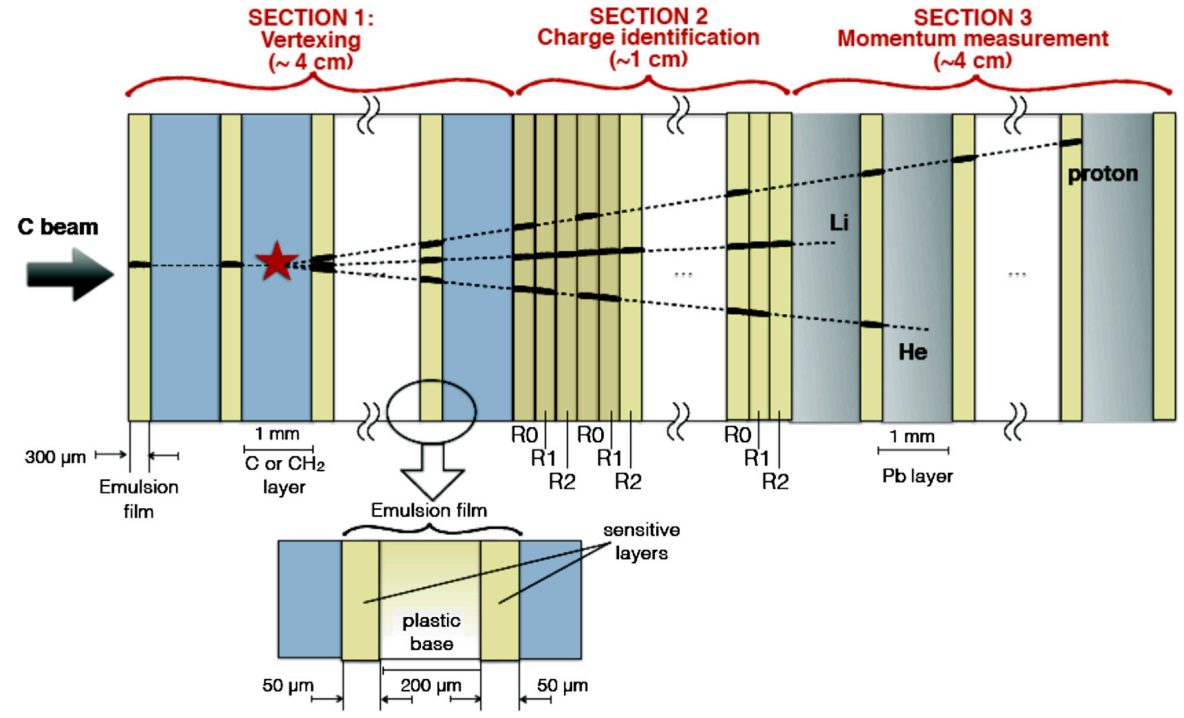

FIGURE 19 | Schematic overview of the ECC layout. Drawing is not to scale.

available at FAIR. These data will answer many questions raised so far and they will validate the models used in various simulation tools.

Some modeling approaches for ^{4}He total reaction and ^{3}He production cross sections were presented in **section 3.2.2**. More experimental data for the other reaction channels (production of ^{1}H, ^{2}H, ^{3}H, and neutrons) are required to improve the modeling.

Recent experiments pointed out problems with dose calculation in the beam halo of ^{4}He ions [33]. Those may be improved by optimization of ^{4}He nuclear models against double differential cross sections.

Although double differential cross section models are preferred for comparisons to experimental data, accurate total reaction and fragmentation cross sections are also needed by radiation transport codes for prediction of particle fluences. Moreover, total fragmentation cross section models can be used for normalizing and anchoring parametric models, such as DDFRG [12, 13, 119]. Werneth et al. [146–150] developed a relativistic (kinematics) multiple scattering theory (RMST) for the prediction of reaction, elastic, total, and elastic differential cross sections for space radiation–relevant reactions. The fundamental nuclear constituents of the MST are defined as the nucleons, and the quark structure of individual nucleons is not considered. Consequently, the interaction of nucleon–nucleus and nucleus–nucleus reaction is modeled as the sum of nucleon–nucleon interactions, which may be parameterized to free nucleon–nucleon transition amplitudes. Elastic differential, total, reaction, and elastic cross sections may be found by solving the Lippmann–Schwinger (LS) equation or with a high-energy, small angle approximation known as the Eikonal approximation. Relativistic kinematics are easily incorporated into the momentum–space formulation of the LS equation [146, 147], and a large shift toward small angles and with larger magnitude is observed in the elastic differential cross sections. Another interesting result is that relativistic kinematic effects will depend on both energy and relative mass of the projectile and target [148]. A comprehensive validation effort [149] showed that the

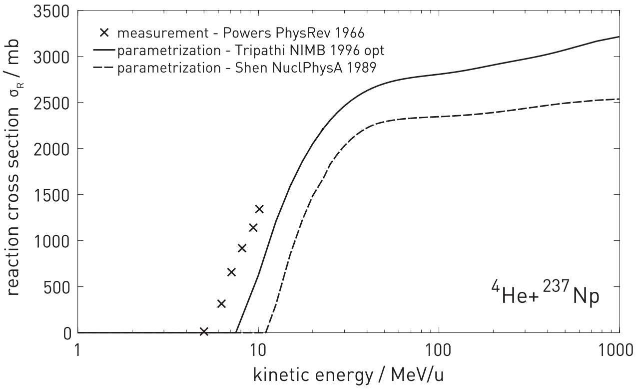

FIGURE 20 | Experimental data of total reaction cross sections for ^{4}He-induced reactions on ^{237}Np targets, compared with two different parameterizations. The parameterizations shown are by Tripathi et al. [109] with the modifications described by Horst et al. [43] and the parameterization by Shen et al. [110] with the modifications proposed by Sihver et al. [111]. The experimental data taken are from Powers et al. [73].

relativistic three dimensional LS model (LS3D) agrees best with experimental data. Additional model improvements led to LS3D predictions of the reaction cross sections that were of the same fidelity to data as the Tripathi parameterizations [150]. In order to improve computational efficiency, a momentum–space formulation of the Eikonal approximation was developed.

The relativistic abrasion–ablation de-excitation fragmentation (RAADFRG) model has been formulated for fragments produced from nucleus–nucleus collisions by coupling the highly efficient Eikonal model for nuclear abrasion to a de-excitation model described by the Weisskopf–Ewing mechanism. Relativistic kinematics may be incorporated by renormalizing the sum of the Eikonal abrasion cross sections to the reaction cross section produced from the LS3D theory. As the projectile nucleus collides with a target nucleus, nucleons are sheared away from the projectile and target during a very short time scale, leaving the pre-fragment (remaining projectile nuclear constituents) in an excitation state. The pre-fragment is assigned an excitation energy, which may include multiple scattering and energy depositions from nucleon–nucleon collisions. After a much longer time scale, the excited pre-fragment will emit light ions and neutrons with probabilities described by the Weisskopf–Ewing formalism until all available excitation energy is exhausted. Nuclear structure is manifested in the fragmentation cross sections with proper choice of the nuclear partition function and excitation energy model. Furthermore, RAADFRG may be used to anchor parametric double differential cross section models such as DDFRG [12, 13, 119]. The dearth of experimental light ion fragmentation data makes it difficult to fully validate the RAADFRG model and other nuclear models that are needed for space radiation applications.

Finally, another modeling activity required in future is to confirm the SHIELD double differential cross section results for light ion production from He projectiles, shown in **Figure 15**. Comparisons need to be made with other cross section models.

7 SUMMARY AND CONCLUSION

Helium projectile double differential cross sections for the production of neutrons and light ions are of great importance to space radiation and ion therapy studies. However, transport codes and cross section models display significant problems when compared with limited data on both thick and thin targets. Also, there is a very significant lack of high-quality experimental data available that could resolve these problems. The following recommendations are made:

- A new set of inclusive, isotopic, double differential cross sections should be measured for a complete set of neutron and light ion fragments for the reactions

$$^4\mathrm{He} + \mathrm{H, C, O, Ca, Al, Fe} \rightarrow \mathrm{n},{}^{1,2,3}\mathrm{H},{}^{3,4}\mathrm{He} + \mathrm{X}$$

- for projectile kinetic energies ranging over 50 MeV/n–50 GeV/n and fragment angles ranging over 0°–180°.
- Those experiments should be accompanied by measurements of total reaction and single differential fragment production cross sections for ^{4}He projectiles, in particular for targets heavier than oxygen in the energy range between 50 MeV/n–50 GeV/n and at energies around the Coulomb barrier.
- A parallel program of cross section model development needs to be initiated in order to develop accurate models for these new measurements.
- A parallel program of transport code validation needs to be undertaken.

The present work has focused on helium projectiles because they represent the highest priority. Nevertheless, other projectiles, such as C, O, Si, and Fe are important for both ion therapy and space radiation, as discussed in **Section 1.3**. A program similar to that described above would be very worthwhile for these other projectiles, as summarized by **Eq. 1**.

AUTHOR CONTRIBUTIONS

All authors contributed to the planning, ideas, debating, writing, and editing of the manuscript.

ACKNOWLEDGMENTS

We wish to thank Laura Bagnale (Federico II University, Naples, Italy) for help with data analysis and collection, and Dr. Steve Smith (NASA Langley) for reviewing the manuscript. Bocchini, Giraudo, and Santin were partially supported by the European Space Agency under contract Number 4000125785 ("ROSSINI 3"). Experiments with He ions are performed in Cave A at GSI in the framework of FAIR Phase-0 supported by the GSI Helmholtzzentrum für Schwerionenforschung in Darmstadt (Germany).

REFERENCES

1. Norbury JW, Miller J, Adamczyk AM, Heilbronn LH, Townsend LW, Blattnig SR, et al. Nuclear data for space radiation. *Radiat Meas.* (2012) 47:315–63. doi:10.1016/j.radmeas.2012.03.004.
2. Norbury JW, Miller J, Adamczyk A, Heilbronn L, Townsend L, Blattnig S, et al. Review of nuclear physics experiments for space radiation. NASA Technical Paper, NASA/TP-2011-217179, National Aeronautics and Space Administration, Washington DC (2011)
3. Norbury JW. Nuclear physics and space radiation. *J Phys Conf Ser.* (2012) 381: 012117. doi:10.1088/1742-6596/381/1/012117.
4. Norbury JW, Miller J. Review of nuclear physics experimental data for space radiation. *Health Phys.* (2012) 103:640–2. doi:10.1097/hp.0b013e318261fb7f.
5. Rutherford E. The scattering of α and β particles by matter and the structure of the atom. *Phil Mag.* (1911) 21:669–688. doi:10.1080/14786440508637080.
6. Tommasino F, Scifoni E, Durante M. New ions for therapy. *Int J Particle Therapy.* (2015) 2:428–38. doi:10.14338/ijpt-15-00027.1.

7. Norbury JW, Slaba TC, Aghara S, Badavi FF, Blattnig SR, Clowdsley MS, et al. Advances in space radiation physics and transport at NASA. *Life Sci Space Res.* (2019) 22:98–124. doi:10.1016/j.lssr.2019.07.003.
8. Walker SA, Townsend LW, Norbury JW. Heavy ion contributions to organ dose equivalent for the 1977 galactic cosmic ray spectrum. *Adv Space Res.* (2013) 51: 1792–1799. doi:10.1016/j.asr.2012.12.011.
9. Norbury JW, Slaba TC. Space radiation accelerator experiments - the role of neutrons and light ions. *Life Sci Space Res.* (2014) 3:90–4. doi:10.1016/j.lssr.2014.09.006.
10. Slaba TC, Blattnig SR, Norbury JW, Rusek A, La Tessa C. Reference field specification and preliminary beam selection strategy for accelerator-based GCR simulation. *Life Sci Space Res.* (2016) 8:52–67. doi:10.1016/j.lssr.2016.01.001.
11. Wilson JW, Slaba TC, Badavi FF, Reddell BD, Bahadori AA. Advances in NASA radiation transport research: 3DHZETRN. *Life Sci Space Res.* (2014) 2: 6–22. doi:10.1016/j.lssr.2014.05.003.
12. Norbury JW, Latysheva L, Sobolevsky N. Light ion double-differential cross section parameterizations and results from the SHIELD transport code. *Nucl Instrum Methods Phys Res A.* (2019) 947:162576. doi:10.1016/j.nima.2019.162576.
13. Norbury JW. *Light ion double-differential cross sections for space radiation.* NASA Technical Publication, NASA/TP-2018-220077, National Aeronautics and Space Administration, Washington DC (2018)
14. Norbury JW, Slaba TC, Sobolevsky N, Reddell B. Comparing HZETRN, SHIELD, FLUKA and GEANT transport codes. *Life Sci Space Res.* (2017) 14:64–73. doi:10.1016/j.lssr.2017.04.001.
15. Slaba TC, Bahadori AA, Reddell BD, Singleterry RC, Clowdsley MS, Blattnig SR. Optimal shielding thickness for galactic cosmic ray environments. *Life Sci Space Res.* (2017) 12: 1–15. doi:10.1016/j.lssr.2016.12.003.
16. Beach M, Castellanos L, Clowdsley M, Heilbronn L, La Tessa C, McGirl N, et al. Double differential light ion production cross sections from 300 AMeV oxygen and 600 AMeV iron beams on aluminum, carbon and polyethylene targets. *Nucl Instrum Methods Phys Res B.* (submitted).
17. Sato T, Niita K, Matsuda N, Hashimotot S, Iwamoto Y, Noda S, et al. Particle and heavy ion transport code system PHITS, version 2.52. *J Nucl Sci Technol.* (2013) 50:913–23. doi:10.1080/00223131.2013.814553.
18. Heilbronn H, et al. to be published.
19. Matthiä D, Ehresmann B, Lohf H, Köhler J, Zeitlin C, Appel J, et al. The Martian surface radiation environment - a comparison of models and MSL/RAD measurements. *J. Space Weather Space Clim.* (2016) 6:A13. doi:10.1051/swsc/2016008.
20. Hassler DM, Norbury JW, Reitz G. Mars science laboratory radiation assessment detector (MSL/RAD) modeling workshop proceedings. *Life Sci Space Res.* (2017) 14:1–2. doi:10.1016/j.lssr.2017.06.004.
21. Matthiä D, Hassler DM, de Wet W, Ehresmann B, Firan A, Flores-McLaughlin J, et al. The radiation environment on the surface of Mars - summary of model calculations and comparison to RAD data. *Life Sci Space Res.* (2017) 14:18–28. doi:10.1016/j.lssr.2017.06.003.
22. Slaba TC, Blattnig SR, Badavi FF, Stoffle NN, Rutledge RD, Lee KT, et al. Statistical validation of HZETRN as a function of vertical cutoff rigidity using ISS measurements. *Adv Space Res.* (2011) 47:600–10. doi:10.1016/j.asr.2010.10.021.
23. Slaba TC, Blattnig SR, Reddell B, Bahadori A, Norman RB, Badavi FF. Pion and electromagnetic contribution to dose: comparisons of HZETRN to Monte Carlo results and ISS data. *Adv Space Res.* (2013) 52:62–78. doi:10.1016/j.asr.2013.02.015.
24. Battistoni G, Mattei I, Muraro S. Nuclear physics and particle therapy. *Adv Phys X.* (2016) 1:661–86. doi:10.1080/23746149.2016.1237310.
25. Durante M, Paganetti H. Nuclear physics in particle therapy: a review. *Rep Prog Phys.* (2016) 79:096702. doi:10.1088/0034-4885/79/9/096702.
26. Zeitlin C, La Tessa C. The role of nuclear fragmentation in particle therapy and space radiation protection. *Front. Oncol.* (2016) 6:1–13. doi:10.3389/fonc.2016.00065.
27. Parodi K, Mairani A, Brons S, Hasch BG, Sommerer F, Naumann J, et al. Monte Carlo simulations to support start-up and treatment planning of scanned proton and carbon ion therapy at a synchrotron-based facility. *Phys Med Biol.* (2012) 57:3759–84. doi:10.1088/0031-9155/57/12/3759.
28. Battistoni G, Bauer J, Boehlen TT, Cerutti F, Chin MPW, Dos Santos Augusto R, et al. The FLUKA code: an accurate simulation tool for particle therapy. *Front Oncol.* (2016) 6:1–24. doi:10.3389/fonc.2016.00116.
29. Krämer M, Jäkel O, Haberer T, Kraft G, Schardt D, Weber U. Treatment planning for heavy-ion radiotherapy: physical beam model and dose optimization. *Phys Med Biol 60th Anniversary Collection.* (2016) 37.
30. Haettner E, Iwase H, Krämer M, Kraft G, Schardt D. Experimental study of nuclear fragmentation of 200 and 400 MeV/u12C ions in water for applications in particle therapy. *Phys Med Biol.* (2013) 58(23):8265–8279. doi:10.1088/0031-9155/58/23/8265.
31. Krämer M, Scifoni E, Schuy C, Rovituso M, Tinganelli W, Maier A, et al. Helium ions for radiotherapy? Physical and biological verifications of a novel treatment modality. *Med Phys.* (2016) 43:1995–2004. doi:10.1118/1.4944593.
32. Sokol O, Scifoni E, Tinganelli W, Kraft-Weyrather W, Wiedemann J, Maier A, et al. Oxygen beams for therapy: advanced biological treatment planning and experimental verification. *Phys Med Biol.* (2017) 62:7798–813. doi:10.1088/1361-6560/aa88a0.
33. Tessonnier T, Mairani A, Brons S, Sala P, Cerutti F, Ferrari A, et al. Helium ions at the Heidelberg ion beam therapy center: comparisons between FLUKA Monte Carlo code predictions and dosimetric measurements. *Phys Med Biol.* (2017) 62:6784. doi:10.1088/1361-6560/aa7b12.
34. Robert C, Dedes G, Battistoni G, Böhlen TT, Buvat I, Cerutti F, et al. Distributions of secondary particles in proton and carbon-ion therapy: a comparison between GATE/Geant4 and FLUKA Monte Carlo codes. *Phys Med Biol.* (2013) 58:2879. doi:10.1088/0031-9155/58/9/2879.
35. Kase Y, Kanematsu N, Kanai T, Matsufuji N. Biological dose calculation with Monte Carlo physics simulation for heavy-ion radiotherapy. *Phys Med Biol.* (2006) 51:N467. doi:10.1088/0031-9155/51/24/n03.
36. Piersanti L, Bellini F, Bini F, Collamati F, De Lucia E, Durante M, et al. Measurement of charged particle yields from PMMA irradiated by a 220 MeV/u12Cbeam. *Phys Med Biol.* (2014) 59:1857. doi:10.1088/0031-9155/59/7/1857.
37. Lühr A, Hansen DC, Teiwes R, Sobolevsky N, Jäkel O, Bassler N. The impact of modeling nuclear fragmentation on delivered dose and radiobiology in ion therapy. *Phys Med Biol.* (2012) 57:5169–85. doi:10.1088/0031-9155/57/16/5169.
38. Kodaira S, Kitamura H, Kurano M, Kawashima H, Benton ER. Contribution to dose in healthy tissue from secondary target fragments in therapeutic proton, He and C beams measured with CR-39 plastic nuclear track detectors. *Sci Rep..* (2019) 9:3708. doi:10.1038/s41598-019-39598-0.
39. Dudouet J, Juliani D, Labalme M, Cussol D, Angélique JC, Braunn B, et al. Double-differential fragmentation cross-section measurements of 95 MeV/n ^{12}C beams on thin targets for hadron therapy. *Phys Rev C.* (2013) 88:24606. doi:10.1103/physrevc.88.024606.
40. Dudouet J, Juliani D, Labalme M, Cussol D, Angélique JC, Braunn B, et al. Erratum: double-differential fragmentation cross-section measurements of 95 MeV/n ^{12}C beams on thin targets for hadron therapy. *Phys Rev C.* (2014) 89: 069904. doi:10.1103/physrevc.89.069904.
41. Divay C, Colin J, Cussol D, Finck Ch, Karakaya Y, Labalme M, et al. Differential cross section measurements for hadron therapy: 50 MeV/n ^{12}C reactions on H, C, O, Al, and natTi targets. *Phys Rev C.* (2017) 95:044602. doi:10.1103/physrevc.95.044602.
42. Horst F, Schuy C, Weber U, Brinkmann KT, Zink K. Measurement of charge- and mass-changing cross sections for ^{4}He + ^{12}C collisions in the energy range 80 - 220 MeV/n for applications in ion beam therapy. *Phys Rev C.* (2017) 96: 024624. doi:10.1103/physrevc.96.024624.
43. Horst F, Aricó G, Brinkmann KT, Brons S, Ferrari A, Haberer T, et al. Measurement of ^{4}He charge- and mass-changing cross sections on H, C, O, and Si targets in the energy range 70 - 220 MeV/n for radiation transport calculations in ion-beam therapy. *Phys Rev C.* (2019) 99:014603. doi:10.1103/physrevc.99.014603.
44. Datta K, Suman S, Kallakury B, Fornace A. Exposure to heavy ion radiation induces persistent oxidative stress in mouse intestine. *PloS One.* (2012) 7: e42224. doi:10.1371/journal.pone.0042224.
45. Mewaldt RA, Cohen CMS, Labrador AW, Leske RA, Mason GM, Desai MI, et al. Proton, helium, and electron spectra during the large solar particle events of October-November 2003. *J Geophys Res.* (2005) 110:A09S18. doi:10.1029/2005ja011038.
46. Slaba TC, Blattnig SR. GCR environmental models I: sensitivity analysis for GCR environments. *Space Weather.* (2014) 12:217–24. doi:10.1002/2013sw001025.

47. Bocchini L, et al. To be published.
48. Santin G, Ivanchenko V, Evans H, Nieminen P, Daly E. GRAS: a general-purpose 3-D modular simulation tool for space environment effects analysis. *IEEE Trans Nucl Sci.* (2005) 52(6):2294–2299. doi:10.1109/tns.2005.860749.
49. Dietze G, Bartlett DT, Cool DA, Cucinotta FA, Jia X, McAulay IR, et al. ICRP publication 123: assessment of radiation exposure of astronauts in space. *Ann ICRP.* (2013) 42(4):1–339. doi:10.1016/j.icrp.2013.05.004.
50. Giraudo M, Schuy C, Weber U, Rovituso M, Santin G, Norbury JW, et al. Accelerator-based tests of shielding effectiveness of different materials and multilayers using high-energy light and heavy ions. *Radiat Res.* (2018) 190(5): 526–37. doi:10.1667/rr15111.1.
51. Castro JR, Char DH, Petti PL, Daftari IK, Quivey JM, Singh RP, et al. 15 years experience with helium ion radiotherapy for uveal melanoma. *Int J Radiat Oncol Biol Phys.* (1997) 39:989–996. doi:10.1016/s0360-3016(97)00494-x.
52. Pedroni E, Böhringer T, Coray A, Egger E, Grossmann M, Lin S, et al. Initial experience of using an active beam delivery technique at PSI. *Strahlenther Onkol.* (1999) 175:18–20. doi:10.1007/bf03038879.
53. Schardt D, Elsässer T, Schulz-Ertner D. Heavy-ion tumor therapy: physical and radiobiological benefits. *Rev Mod Phys.* (2010) 82:383. doi:10.1103/revmodphys.82.383.
54. Kamada T, Tsujii H, Blakely EA, Debus J, De Neve W, Durante M, et al. Carbon ion radiotherapy in Japan: an assessment of 20 years of clinical experience. *Lancet Oncol.* (2015) 16:e93-e100. doi:10.1016/s1470-2045(14)70412-7.
55. Knäusl B, Fuchs H, Dieckmann K, Georg D. Can particle beam therapy be improved using helium ions? - a planning study focusing on pediatric patients. *Acta Oncologica..* (2016) 55:751–759. doi:10.3109/0284186x.2015.1125016.
56. Tessonnier T, Mairani A, Chen W, Sala P, Cerutti F, Ferrari A, et al. Proton and helium ion radiotherapy for meningioma tumors: a Monte Carlo-based treatment planning comparison. *Rad. Oncol.* (2018) 13:2. doi:10.1186/s13014-017-0944-3.
57. Grün R, Friedrich T, Krämer M, Zink K, Durante M, Engenhart-Cabillic R, et al. Assessment of potential advantages of relevant ions for particle therapy: a model based study. *Med Phys.* (2015) 42:1037–47. doi:10.1118/1.4905374.
58. Inaniwa T, Suzuki M, Hyun Lee S, Mizushima K, Iwata Y, Kanematsu N, et al. Experimental validation of stochastic microdosimetric kinetic model for multi-ion therapy treatment planning with helium-, carbon-, oxygen-, and neon-ion beams. *Phys Med Biol.* (2020) 65:045005. doi:10.1088/1361-6560/ab6eba.
59. Sokol O, Krämer M, Hild S, Durante M, Scifoni E. Kill painting of hypoxic tumors with multiple ion beams. *Phys Med Biol.* (2019) 64:045008. doi:10.1088/1361-6560/aafe40.
60. Schneider T, Patriarca A, Prezado Y. Improving the dose distributions in minibeam radiation therapy: helium ions vs protons. *Med Phys.* (2019) 46: 3640–3648. doi:10.1002/mp.13646.
61. Gehrke T, Amato C, Berke S, Martisikova M. Theoretical and experimental comparison of proton and helium-beam radiography using silicon pixel detectors. *Phys Med Biol.* (2018) 63:035037. doi:10.1088/1361-6560/aaa60f. |
62. Volz L, Kelleter L, Brons S, Burigo LN, Graeff C, Niebuhr NI, et al. Experimental exploration of a mixed helium/carbon beam for online treatment monitoring in carbon ion beam therapy. *Phys Med Biol.* (2020) 65:055002. doi:10.1088/1361-6560/ab6e52.
63. Ingemarsson A, Nyberg J, Renberg PU, Sundberg O, Carlson RF, Cox AJ, et al. New results for reaction cross sections of intermediate energy α-particles on targets from Be to Pb. *Nucl Phys.* (2000) 676:3–31. doi:10.1016/s0375-9474(00)00200-1.
64. DeVries RM, DiGiacomo NJ, Kapustinsky JS, Peng JC, Sondheim WE, Sunier JW, et al. Dominance of nucleon-nucleon interactions inα+C12total reaction cross sections. *Phys Rev C.* (1982) 26:301. doi:10.1103/physrevc.26.301.
65. Tanihata I, Hamagaki H, Hashimoto O, Nagamiya S, Shida Y, Yoshikawa N, et al. Measurements of interaction cross sections and radii of He isotopes. *Phys Lett B.* (1985) 160:380–384. doi:10.1016/0370-2693(85)90005-x.
66. Jaros J, Wagner A, Anderson L, Chamberlain O, Fuzesy RZ, Gallup J, et al. Nucleus-nucleus total cross sections for light nuclei at 1.55 and 2.89 GeV/cper nucleon. *Phys Rev C.* (1978) 18:2273. doi:10.1103/physrevc.18.2273.
67. Aksinenko VD, Anikina MKh, Buttsev VS, Chkaidze LV, Glagoleva NS, Golokhvastov AI, et al. Streamer chamber study of the cross sections and multiplicities in nucleus-nucleus interactions at the incident momentum of 4.5 GeV/c per nucleon. *Nucl Phys.* (1980) 348:518–34. doi:10.1016/0375-9474(80)90269-9.
68. Warner RE, Patty RA, Voyles PM, Nadasen A, Becchetti FD, Brown JA, et al. Total reaction and 2n-removal cross sections of 20-60AMeVHe4,6,8,Li6-9,11, andBe10on Si. *Phys Rev C.* (1996) 54:1700. doi:10.1103/physrevc.54.1700.
69. Sourkes AM, Houdayer A, van Oers WTH, Carlson RF, Brown Ronald E Total reaction cross section for protons onHe3andHe4between 18 and 48 MeV. *Phys Rev C.* (1976) 13:451. doi:10.1103/physrevc.13.451.
70. Kozodaev MS, Kulyukin MM, Sulyaev RM, Filippov AI, Shcherbakov Yu.A Interactions between 630 MeV protons and ^{4}He nuclei. *Sov Phys JETP.* (1960) 38:511–516.
71. Neumaier SR, Alkhazov GD, Andronenko MN, Dobrovolsky AV, Egelhof P, Gavrilov GE, et al. Small-angle proton elastic scattering from the neutron-rich isotopes 6He and 8He, and from 4He, at 0.7 GeV in inverse kinematics. *Nucl Phys.* (2002) 712:247–268. doi:10.1016/s0375-9474(02)01274-5.
72. Saint-Laurent MG, Anne R, Bazin D, Guillemaud-Mueller D, Jahnke U, Gen MJ, et al. Total cross sections of reactions induced by neutron-rich light nuclei. *Z. Physik A - Atomic Nuclei.* (1989) 332:457–465. doi:10.1007/bf01292431.
73. Powers JA, Wogman NA, Cobble JW. Mass distribution in the fission ofNp237andPu239by intermediate-energy helium ions. *Phys Rev.* (1966) 152:1096. doi:10.1103/physrev.152.1096.
74. Webber WR, Kish JC, Schrier DA. Total charge and mass changing cross sections of relativistic nuclei in hydrogen, helium, and carbon targets. *Phys Rev C.* (1990) 41:520–532. doi:10.1103/physrevc.41.520.
75. Ferrando P, Webber WR, Goret P, Kish JC, Schrier DA, Soutoul A, et al. Measurement ofC12,O16, andFe56charge changing cross sections in helium at high energy, comparison with cross sections in hydrogen, and application to cosmic-ray propagation. *Phys Rev C.* (1988) 37:1490–1501. doi:10.1103/physrevc.37.1490.
76. Igo G, Wilkins BD. Alpha-particle reaction cross sections at 40 MeV. *Phys. Rev.* (1963) 131:1251. doi:10.1103/physrev.131.1251.
77. Labie E, Lega J, Leleux P, Macq PC. Total reaction cross section of α-particles on carbon between 15.8 and 20.1 MeV. *Nucl Phys.* (1973) 205:81–89. doi:10.1016/0375-9474(73)90121-8.
78. Millburn GP, Birnbaum W, Crandall WE, Schecter L. Nuclear radii from inelastic cross-section measurements. *Phys. Rev.* (1954) 95:1268. doi:10.1103/physrev.95.1268.
79. Bilaniuk OMP, Tokarevskii VV, Bulkin VS, Dubar LV, Nemets OF, Slyusarenko LI. Deuteron and alpha-particle total reaction cross sections for nuclei with A~50. *J Phys G Nucl Phys.* (1981) 7:1699. doi:10.1088/0305-4616/7/12/020.
80. Bilaniuk OMP, Tokarevskii VV, Bulkin VS, Dubar LV, Nemets OF, Slyusarenko LI. Fragment mass, energy, and angular distributions for the ^{12}C(^{4}He,heavy ion) reaction between 49 and 159 MeV. *Phys Rev C.* (1984) 29: 1595.
81. Durante M, Cucinotta FA. Physical basis of radiation protection in space travel. *Rev Mod Phys.* (2011) 83:1245. doi:10.1103/revmodphys.83.1245.
82. Auble RL, Ball JB, Bertrand FE, Fulmer CB, Hensley DC, Lee IY, et al. Light ion emission from reactions induced by 0.8-2.4 GeVO16projectiles. *Phys Rev C.* (1983) 28:1552–1564. doi:10.1103/physrevc.28.1552.
83. Fukuda T, Ishihara M, Ogata H, Miura I, Shimoda T, Katori K, et al. Light-particle emission in the reaction of 93Nb + 14N at 132, 159 and 208 MeV. *Nucl Phys.* (1984) 425:548–572. doi:10.1016/0375-9474(84)90023-x.
84. Korejwo A, Giller M, Dzikowski T, Perelygin VV, Zarubin AV. Isotopic cross sections of 12C fragmentation on hydrogen measured at 1.87 and 2.69 GeV/nucleon. *J Phys G Nucl Part Phys.* (2002) 28:1199–208. doi:10.1088/0954-3899/28/6/304.
85. Lindstrom PJ, Greiner DE, Heckman HH, Cork B, Bieser FS. *Isotope production cross sections from the fragmentation of ^{16}O and ^{12}C at relativistic energies.*. LBL-3650 (1975)
86. Nagamiya S, Lemaire MC, Moeller E, Schnetzer S, Shapiro G, Steiner H, et al. Production of pions and light fragments at large angles in high-energy nuclear collisions. *Phys Rev C.* (1981) 24:971–1009. doi:10.1103/physrevc.24.971.

87. Olson DL, Berman BL, Greiner DE, Heckman HH, Lindstrom PJ, Crawford HJ. Factorization of fragment-production cross sections in relativistic heavy-ion collisions. *Phys Rev C.* (1983) 28:1602–1613. doi:10.1103/physrevc.28.1602.
88. Zeitlin C, Miller J, Guetersloh S, Heilbronn L, Fukumura A, Iwata Y, et al. Fragmentation of ^{14}N, ^{16}O, ^{20}Ne, and $_{24}$mg nuclei at 290 to 1000 MeV/n. *Phys Rev C.* (2011) 83:034909. doi:10.1103/physrevc.83.034909.
89. Meyer J. Deuterons and He^3 formation and destruction in proton induced spallation of light nuclei ($Z < = 8$). *Astron AstroPhys Suppl.* (1972) 7:417–467.
90. Abdurakhimov AK, Anikina MK, Buttsev VS, Chikovani LD, Chkhaidze LV, Dementjev EA, et al. A study of pion production in 4.5 GeV/c)/nucleon 4He interactions with nuclear targets. *Nucl Phys.* (1981) 362:376–390. doi:10.1016/0375-9474(81)90500-5.
91. Shibata T, Maeda K, Okada K, Ejiri H, Sakai H, Shimizu A. The pre-equilibrium process of the 165Ho(α, xnγp) reaction at Eγ = 109 MeV studied by particle-gamma coincidence measurements. *Nucl Phys.* (1985) 441:445–460. doi:10.1016/0375-9474(85)90155-1.
92. Gosset J, Gutbrod HH, Meyer WG, Poskanzer AM, Sandoval A, Stock R, et al. Central collisions of relativistic heavy ions. *Phys Rev C.* (1977) 16:629–657. doi:10.1103/physrevc.16.629.
93. Bizard G, Le Brun C, Berger J, Duflo J, Goldzahl L, Plouin F, et al. ^{3}He production in 4He fragmentation on protons at 6.85 GeV/c. *Nucl Phys.* (1977) 285:461–468. doi:10.1016/0375-9474(77)90645-5.
94. Riddiford L, Williams AW. The interaction of 970 MeV protons with helium. *Proc. Roy. Soc. A.* (1960) 257:316–325.
95. Motobayashi T, Ejiri H, Shibata T, Okada K, Sasao M, Maeda K, et al. Breakup process for 100 MeV 3He interacting with 165Ho and 166, 167Er nuclei. *Nucl Phys.* (1984) 413:290–310. doi:10.1016/0375-9474(84)90376-2.
96. Zhu F, Lynch WG, Murakami T, Gelbke CK, Kim YD, Nayak TK, et al. Light particle correlations for theHe3+Ag reaction at 200 MeV. *Phys Rev C.* (1991) 44:R582–R585. doi:10.1103/physrevc.44.r582.
97. Doering RR, Schweizer TC, Thornton ST, Dennis LC, Cordell KR, Ziock KOH, et al. Correlated energy spectra of light fragments from 720-MeVα-induced reactions. *Phys Rev Lett.* (1978) 40:1433–1435. doi:10.1103/physrevlett.40.1433.
98. Anderson LMJ. Fragmentation of relativistic light nuclei: longitudinal and transverse momentum distributions. [0. 93 GeV/c/nucleon, 0. 5 to 11. 5, cross sections, limiting fragmentation, nuclear structure, production mechanism]. *LBL report.* 6769 (1977) doi:10.2172/5335548.
99. Westfall GD, Gosset J, Johansen PJ, Poskanzer AM, Meyer WG, Gutbrod HH, et al. Nuclear fireball model for proton inclusive spectra from relativistic heavy-ion collisions. *Phys Rev Lett.* (1976) 37:1202–1205. doi:10.1103/physrevlett.37.1202.
100. Anderson L, Brückner W, Moeller E, Nagamiya S, Nissen-Meyer S, Schroeder L, et al. Inclusive particle production at forward angles from collisions of light relativistic nuclei: nuclear fragments. *Phys Rev C.* (1983) 28:1224–1245. doi:10.1103/physrevc.28.1224.
101. Banaigs J, Berger J, Berthet P, Bizard G, Boivin M, De Sanctis M, et al. Inelastic scattering ofαparticles on light nuclei atPα=7.0 GeV/c. *Phys Rev C.* (1987) 35:1416–1424. doi:10.1103/physrevc.35.1416.
102. Rovituso M, Schuy C, Weber U, Brons S, Cortés-Giraldo MA, La Tessa C, et al. Fragmentation of 120 and 200 MeV u−14He ions in water and PMMA targets. *Phys Med Biol.* (2017) 62:1310. doi:10.1088/1361-6560/aa5302.
103. Marafini M, Paramatti R, Pinci D, Battistoni G, Collamati F, De Lucia E, et al. Secondary radiation measurements for particle therapy applications: nuclear fragmentation produced by4He ion beams in a PMMA target. *Phys Med Biol.* (2017) 62:1291. doi:10.1088/1361-6560/aa5307.
104. Schuy C, Tessa C, Horst F, Rovituso M, Dyrante M, Giraudo M, et al. Experimental assessment of lithium hydride's space radiation shielding performance and Monte Carlo benchmarking 2019. *Radiat Res.* (2019) 191(2):154–161.
105. Sato H, Kurosawa T, Iwase H, Nakamura T, Uwamino Y, Nakao N Measurements of double differential neutron production cross sections by 135 MeV/nucleon He, C, Ne and 95 MeV/nucleon Ar ions. *Phys Rev C.* (2001) 64:034607. doi:10.1103/physrevc.64.034607.
106. Heilbronn L, Zeitlin CJ, Iwata Y, Murakami T, Iwase H, Nakamura T, et al. Secondary neutron-production cross sections from heavy-ion interactions between 230 and 600 MeV/nucleon. *Nucl Sci Eng.* (2007) 157:142–158. doi:10.13182/nse07-a2719.
107. Krämer M, Scholz M. Treatment planning for heavy-ion radiotherapy: calculation and optimization of biologically effective dose. *Phys Med Biol.* (2000) 45:3319–3330. doi:10.1088/0031-9155/45/11/314. |
108. Tripathi RK, Cucinotta FA, Wilson JW. Accurate universal parameterization of absorption cross sections III - light systems. *Nucl Instrum Methods Phys Res Sect B Beam Interact Mater Atoms.* (1999) 155:349–356. doi:10.1016/s0168-583x(99)00479-6.
109. Tripathi RK, Cucinotta FA, Wilson JW. Accurate universal parameterization of absorption cross sections. *Nucl Instrum Methods Phys Res Sect B Beam Interact Mater Atoms.* (1996) 117:347–349. doi:10.1016/0168-583x(96)00331-x.
110. Shen W-q., Wang B, Feng J, Zhan W-l., Zhu Y-t., Feng E-p.. Total reaction cross section for heavy-ion collisions and its relation to the neutron excess degree of freedom. *Nucl Phys.* (1989) 491:130–146. doi:10.1016/0375-9474(89)90209-1.
111. Sihver L, Lantz M, Kohama A. Improved parameterization of the transparency parameter in Kox and Shen models of total reaction cross sections. *Phys Rev C.* (2014) 89:067602. doi:10.1103/physrevc.89.067602.
112. Sihver L, Kohama A, Ida K, Oyamatsu K, Iwase H, Hashimoto S, et al.. Current status of the Hybrid Kurotama mode for total reaction cross sections. *Nucl Instrum Methods B.* (2014) 334:34–39. doi:10.1016/j.nimb.2014.04.021.
113. Tripathi RK, Wilson JW, Cucinotta FA, Accurate universal parameterization of absorption cross sections II - neutron absorption cross sections. *Nucl Instrum Methods B.* (1997) 129:11–15.
114. Cucinotta FA. *Calculations of cosmic-ray helium transport in shielding materials..* NASA Technical Publication, NASA/TP-3354, National Aeronautics and Space Administration, Washington DC (1993)
115. Aricó G, Ferrari A, Horst F, Mairani A, Reidel CA, Schuy C, et al. Developments of the nuclear reaction and fragmentation models in FLUKA for ion collisions at therapeutic energies. *CERN proc. 1 - 15th international conference on nuclear reaction mechanisms.* (2019)
116. Hüfner J, Schäfer K, Schürmann B. Abrasion-ablation in reactions between relativistic heavy ions. *Phys Rev C.* (1975) 12:1888–98. doi:10.1103/physrevc.12.1888.
117. Tatischeff V, Gabici S. Particle acceleration by supernova shocks and spallogenic nucleosynthesis of light elements. *Annu Rev Nucl Part Sci.* (2018) 68:377–404. doi:10.1146/annurev-nucl-101917-021151.
118. Bartos I. A new cosmic messenger. *Phys World.* (2018) 31:23–26. doi:10.1088/2058-7058/31/1/29.
119. Norbury JW. *DDFRG - double-Differential FRaGmentation models for proton and light ion production in high energy nuclear collisions valid for both small and large angles..* . NASA Technical Publication (in preparation).
120. Nakamura T, Heilbronn L. *Handbook on secondary particle production and transport by high-energy heavy ions..* World Scientific, Singapore (2006)
121. Botvina AS, Dementyev AV, Smirnova ON, Sobolevsky NM, Toneev VD. MSDM - multi stage dynamical model. International codes and model intercomparison for intermediate energy activation yields. In: RR Michel PP Nagel, (Eds.), *NSC/DOC(97)-1.*, NEA/P & T No 14, OECD, Paris, (1997) p. 307.
122. Toneev VD, Gudima KK. Particle emission in light and heavy ion reactions. *Nucl Phys.* (1983) 400:173–189. doi:10.1016/0375-9474(83)90433-5.
123. Amelin NS, Gudima KK, Toneev VD. *Yad Fiz.* (1990) 51:1730, 1990 (in Russian). Preprint GSI-89-52 (in English).
124. Amelin NS, Gudima KK, Siviklokov SY, Toneev VD. *Yad Fiz.* (1990) 52:272, 1990 (in Russian).
125. Gudima KK, Mashnik SG, Toneev VD. Cascade-exciton model of nuclear reactions. *Nucl Phys.* (1983) 401:329–361. doi:10.1016/0375-9474(83)90532-8.
126. Botvina AS, Iljinov AS, Mishustin IN, Bondorf JP, Donangelo R, Sneppen K. Statistical simulation of the break-up of highly excited nuclei. *Nucl Phys.* (1987) 475:663–686. doi:10.1016/0375-9474(87)90232-6.
127. Eren N, Buyukcizmeci N, Ogul R, Botvina AS. Mass distribution in the disintegration of heavy nuclei. *Eur. Phys. J. A.* (2013) 49:48. doi:10.1140/epja/i2013-13048-1.
128. Bondorf JP, Botvina AS, Iljinov AS, Mishustin IN, Sneppen K. Statistical multifragmentation of nuclei. *Phys Rep.* (1995) 257:133–221. doi:10.1016/0370-1573(94)00097-m.

129. Wilson JW, Werneth CM, Slaba TC, Badavi FF, Reddell BD, Bahadori AA. *Effects of the serber first step in 3DHZETRN-v2.1.*. NASA Technical Publication, NASA/TP-2019-220401, National Aeronautics and Space Administration, Washington DC (2019)
130. Valle SM, et al. FOOT: a new experiment to measure nuclear fragmentation at intermediate energies. *Perspect. Sci.* (2019) 12:100415.
131. Pleskac R, Abou-Haidar Z, Agodi C, Alvarez MAG, Aumann T, Battistoni G, et al. The FIRST experiment at GSI. *Nucl Instrum Methods Phys Res Sect A Accel Spectrom Detect Assoc Equip.* (2012) 678:130–138. doi:10.1016/j.nima.2012.02.020.
132. Geissel H, Armbruster P, Behr KH, Brünle A, Burkard K, Chen M, et al. The GSI projectile fragment separator (FRS): a versatile magnetic system for relativistic heavy ions. *Nucl Instrum Methods Phys Res Sect B Beam Interact Mater Atoms.* (1992) 70:286–297. doi:10.1016/0168-583x(92)95944-m.
133. Stöhlker T, Bagnoud V, Blaum K, Blazevic A, Bräuning-Demian A, Durante M, et al. APPA at FAIR: from fundamental to applied research. *Nucl Instrum Methods Phys Res Sect B Beam Interact Mater Atoms.* (2015) 365:680–685. doi:10.1016/j.nimb.2015.07.077.
134. La Tessa C, Sivertz M, Chiang I-H, Lowenstein D, Rusek A. Overview of the NASA space radiation laboratory. *Life Sci Space Res.* (2016) 11:18–23. doi:10.1016/j.lssr.2016.10.002.
135. McGirl N, Castellanos L, Srikrishna A, Heilbronn L, La Tessa C, Rusek A, et al. Double differential neutron yields from thick targets used in space applications. *EPJ Web Conf.* (2017) 158:04002.
136. Kekelidze VD, Matveev VA, Meshkov IN, Sorin AS, Trubnikov GV. Project nuclotron-based ion collider fAcility at JINR. *Phys Part Nucl.* (2017) 48: 727–741. doi:10.1134/s1063779617050239.
137. Kurosawa T, Nakao N, Nakamura T, Uwamino Y, Shibata T, Nakanishi N, et al. Measurements of secondary neutrons produced from thick targets bombarded by high-energy helium and carbon ions. *Nucl Sci Eng.* (1999) 132: 30–57. doi:10.13182/nse98-53.
138. Mattei I, Giuseppina MB, Bruni G, Camarlinghi N, Carra P, Catanzani E, et al. Measurement of ^{12}C fragmentation cross sections on C, O and H in the energy range of interest for particle therapy applications. *IEEE Transactions.* (2020) 4:269–282.
139. Pivi M, de Franco A, Farinon F, Kronberger M, Kronberger M, Kulenkampff T. Overview and status of the MedAustron ion therapy center accelerator. *Proceedings of IPAC2017.* (2017)
140. *FOOT conceptual design report.*, https://pandora.infn.it/public/912bb8
141. Alexandrov A, Alpat B, Ambrosi G, Argirò S, Battistoni G, Bisogni MG, et al. The FOOT (fragmentation of target) experiment. *PoS.* (BORMIO2017) (2017) :023.
142. Argiro S, Barbosa D, Battistoni G, Belcari N, Bruni G, Giuseppina MB, et al. The FOOT (fragmentation of target) experiment. *PoS.* (2016) :128.
143. Ferrari A, Sala PR, Fassò A, Ranft J. *FLUKA: a multi-particle transport code.*. CERN-2005-10 (2005) INFN/TC_05/11, SLAC-R-773.
144. Böhlen TT, Cerutti F, Chin MPW, Fassò A, Ferrari PG, Ortega A, et al. The FLUKA code: developments and challenges for high energy and medical applications. *Nucl Data Sheets.* (2014) 120:211–214. doi:10.1016/j.nds.2014.07.049.
145. Alexandrov A, et al. The FOOT experiment: fragmentation measurements in particle therapy. *Rad. Applic.* (2018) 3(3):190–6.
146. Werneth CM, Maung KM, Ford WP, Norbury JW, Vera MD. Elastic differential cross sections for space radiation applications. *Phys Rev C.* (2014) 90:064905. doi:10.1103/physrevc.90.064905.
147. Werneth CM, Maung KM, Ford WP, Norbury JW, Vera MD. *Elastic differential cross sections.*. NASA Technical Publication, NASA/TP-2014-218529, National Aeronautics and Space Administration, Washington DC (2014)
148. Werneth CM, Maung KM, Ford WP. Relativistic elastic differential cross sections for equal mass nuclei. *Phys Lett B.* (2015) 749:331–336. doi:10.1016/j.physletb.2015.08.002.
149. Werneth CM, Xu X, Norman RB, Ford WP, Maung KM. Validation of elastic cross section models for space radiation applications. *Nucl Instrum Methods Phys Res B.* (2017) 392:79–93. doi:10.1016/j.nimb.2016.12.009.
150. Werneth CM, Xu X, Norman RB, Maung KM, Maung KM. Relativistic three-dimensional Lippmann-Schwinger cross sections for space radiation applications. *Nucl Instrum Methods Phys Res Sect B Beam Interact Mater Atoms.* (2017) 413:75–78. doi:10.1016/j.nimb.2017.10.016.

Conflict of Interest: Author CZ was employed by the company "Leidos Innovations Corporation". Authors MG and LB were employed by the company "Thales Alenia Space".

The remaining authors declare that the research was conducted in the absence of any commercial or financial relationships that could be construed as a potential conflict of interest.